

# **Emergence of cellular nematic order is a conserved feature of gastrulation in animal embryos**

Xin Li<sup>1</sup>, Robert J. Huebner<sup>2</sup>, Margot L.K. Williams<sup>3,4</sup>, Jessica Sawyer<sup>5,6</sup>, Mark Peifer<sup>6</sup>, John B. Wallingford<sup>2</sup>, and D. Thirumalai<sup>1,7</sup>

1. Department of Chemistry, University of Texas at Austin, Austin, TX 78712, USA
2. Department of Molecular Bioscience, University of Texas at Austin, Austin, TX 78712, USA
3. Center for Precision Environmental Health & Department of Molecular and Cellular Biology, Baylor College of Medicine, Houston, TX 77030, USA
4. Department of Developmental Biology, Washington University School of Medicine, St. Louis, MO 63110, USA
5. Department of Pharmacology and Cancer Biology, Duke University, Durham, NC 27710, USA
6. Department of Biology, University of North Carolina at Chapel Hill, Chapel Hill, NC 27599-3280, USA
7. Department of Physics, University of Texas at Austin, Austin, TX 78712, USA

## Abstract

Cells undergo dramatic changes in morphology during embryogenesis, yet how these changes affect the formation of ordered tissues remains elusive. Here we find that the emergence of a nematic liquid crystal phase occurs in cells during gastrulation in the development of embryos of fish, frogs, and fruit flies. Moreover, the spatial correlations in all three organisms are long-ranged and follow a similar power-law decay ( $y \sim x^{-\alpha}$ ) with  $\alpha$  less than unity for the nematic order parameter, suggesting a common underlying physical mechanism unifies events in these distantly related species. All three species exhibit similar propagation of the nematic phase, reminiscent of nucleation and growth phenomena. Finally, we use a theoretical model along with disruptions of cell adhesion and cell specification to characterize the minimal features required for formation of the nematic phase. Our results provide a framework for understanding a potentially universal features of metazoan embryogenesis and shed light on the advent of ordered structures during animal development.

# Introduction

During animal embryogenesis, the evolutionarily conserved process of convergent extension (CE) narrows and elongates the body during gastrulation, transforming the largely spherical early embryo into the typical elongated animal body plan with a recognizable head-to-tail axis<sup>1</sup>. CE is driven by directed movement of cells in one axis (convergence), resulting in extension of the perpendicular axis<sup>2,3</sup>. A wealth of descriptive and experimental embryology has characterized the cell biology, molecular controls, and mechanics that underlie CE, across species<sup>4-8</sup>. However, it remains unclear how cellular scale behaviors translate to larger-scale physical transitions.

Confluent cell populations, such as those found in the early embryo, exist in a variety of physical states. For example, a high-density tissue consisting of isotropic, non-proliferative, cells will be in a jammed or solid-like state<sup>9</sup>. In contrast, a growing tissue undergoing dramatic morphological changes must be in a more fluid-like or unjammed state<sup>10</sup>. Transitions between such states are influenced by a variety of parameters, including cell density, proliferation, packing order, and, of particular interest here, cell shape<sup>11-14</sup>. Indeed, dramatic changes in cell shape and cell orientation are a defining feature of vertebrate CE, with cells becoming strikingly aligned and elongated in the axis perpendicular to the elongating head-to-tail axis<sup>15-18</sup>. However, the relationship between cell shape, orientation, and the physical state of tissues during CE has not been defined.

Here, we used zebrafish, *Xenopus*, and *Drosophila* as model systems, to consider CE across a range of organisms. We first find that in all three species, an ordered phase emerges with orientational order arising before overt changes in cell shape. Tissues then transition to a nematic liquid crystal phase defined by long-range orientational order and fluid flow. The emergent long-ranged spatial correlation is characterized by power-law ( $y \sim x^{-\alpha}$ ), with  $\alpha$  being less than unity, during the development of the liquid crystalline phase. Further, we found that each organism exhibited propagation of the nematic phase over time and space could be described by a nucleation-type mechanism. Theoretical modeling suggests a requirement for both local and global cell alignment during nematic phase formation, an idea we tested *in vivo*. Together, our results provide a physical description of how cells acquire an anisotropic liquid crystal state during early embryogenesis and suggests a potentially universal physical mechanism in the CE of evolutionarily distant animals.

# Results and Discussion

## Evolution of anisotropic cell shape during zebrafish gastrulation.

Zebrafish elongate their head-to-tail axis, in part, through convergence and extension of the dorsal mesoderm which gives rise to the notochord<sup>4</sup>. At early stages the presumptive notochord appears as a hexagonally packed confluent tissue (Fig.1a, Supp. Fig.1a-d). Over time, the packing density increases, the mean cell area decreases (Supp. Fig.1e-g and k-m, Supp. Fig.2), and cells become increasingly elongated, particularly in the notochord (dashed lines) (Fig.1b, Supp. Fig.1k-m and Video I). From these largely expected observations<sup>18</sup>, we began a deeper investigation of cell anisotropy.

For a more granular view of cell shape changes, we calculated the shape index  $SI \equiv P/\sqrt{(4\pi A)}$ , where  $P$  is the perimeter and  $A$  is the area of each cell<sup>14</sup>. This parameter has been used to investigate onset of tissue fluidization, because  $SI$  increases as cells become increasingly anisotropic and the tissue becomes more liquid-like<sup>14,20</sup>. The value of  $SI$  is unity for a circle and exceeds unity for other shapes. We collected time-lapse movies of zebrafish CE and assessed the  $SI$  of the cells in the notochord (dashed rectangle) and the surrounding mesoderm (Fig.1a-b).  $SI$  was plotted as a function of position on the mediolateral axis, perpendicular to the head-to-tail axis, to visualize the spatial evolution of cell shape (Supp. Fig.1h-j, n-p). We observed a general increase in  $SI$  across the tissue over time with a particularly strong increase in the notochord region (Supp. Fig.1n-p and Video II). The boxplot in Fig. S1(q) (also Fig. S1(r)) shows that cell shape is significantly different between cells in and outside of the notochord regions. This result demonstrates the formation of a heterogeneous tissue in which cells with different shapes coexist.

To probe the temporal dynamics of cell shape, we calculated the time dependence of the  $SI$  for cells in the notochord. Initially, there is a linear relationship between  $SI$  and time ( $t$ ), indicating a slow increase in the cell shape anisotropy (Fig.1c dark yellow line). However, there is a sharp transition to a steeper slope (an increase of  $\sim 50\%$ ) around  $t=120$  min (Fig.1c red line), which occurs concurrently with the appearance of the notochord boundary (Supp. Fig.1k-p). These data highlight the sensitivity of the  $SI$ , as spatial analysis clearly shows a peak in the notochord region and temporal analysis identified boundary formation through a slope change in the rate.  $SI$  is therefore a sensitive parameter for describing the structural transition in tissues during CE *in vivo*.

## Emergence of a nematic phase during zebrafish gastrulation.

We next asked how cell alignment arises. We first quantified these cells' orientational order, which refers to the alignment of rod-like objects in a particular direction; in this case the arrangement of the long axis of the cell in the tissue (short lines Fig.1d, g at different times). Each line is color-coded by the angle ( $|\theta|$ , see the color bar and the inset in Fig.1d, Supp. Fig.3a) with respect to the mediolateral axis. The polar histogram of  $\theta$  (Supp. Fig.3b) shows a peak around zero degrees, revealing that many cells are aligned along the mediolateral axis even at early times. This trend becomes even more apparent at later

times when almost all the cells in the notochord region orient their long axes along the mediolateral axis (grey dashed rectangle Supp. Fig.3c). The histogram of  $\theta$  (Supp. Fig.3d), and the inset (showing the distribution for cells in the dashed rectangle in Supp. Fig.3c) provide additional support for orientational order.

The highly oriented, elongated cells are reminiscent of the nematic liquid crystal phase. Nematic liquids can flow like a liquid (i.e. without long-range positional order) while retaining long-range orientational order<sup>21</sup>. Liquid crystal states have been used to describe biological structures such as DNA, cytoskeletal elements, and even confluent sheets of cultured epithelial cells<sup>22-25</sup> but have not been implicated in tissue transformations during animal development.

We quantified the orientational order of cells during zebrafish CE in two dimensions (2D) (Fig.1d, g) by calculating the nematic order parameter<sup>21</sup>,

$$S = \langle 2\cos^2\theta - 1 \rangle, \quad (1)$$

where  $\theta$  is the angle shown in Fig. 1(d), and (g). In a perfect nematic liquid, in which all the cells are oriented in the same direction,  $S=1$ , whereas  $S=0$  if cells are randomly oriented.

Due to the spatial heterogeneity and anisotropic nature of the zebrafish tissues, we calculated the value of  $S$  along the mediolateral and anteroposterior directions separately (Fig.1e-f, h-i). The presence of a nematic phase is evident at very early times (see the pink line in the center region in Fig.1f), which is located just as the notochord structure is being established. The nematic order in the notochord region is further enhanced at subsequent times, leading to larger  $S$  values (approaching unity, see the pink line in the center right region in Fig.1i). The large  $S$  value along the anteroposterior axis (Fig.1e)) also shows the presence of a nematic phase ( $S \approx 0.5$ ), but its distribution is more homogenous at early times since the notochord spans the entire regime in the anteroposterior direction. Interestingly, there is a gradient in  $S$  along the anteroposterior direction at later times (see the blue line in Fig.1h). It is striking that the value of  $S$  is near unity at  $t = 147$  min in the mediolateral region between  $100 \mu\text{m}$  and  $150 \mu\text{m}$  (Fig. 1i). Even outside this region  $S$  has a non-zero value, showing a dramatic development of the nematic order during the CE.

Our data reveal that cells in the zebrafish notochord adopts a typical nematic phase during CE (see the well-stacked cells in Fig.1g and  $S \approx 1$  in Fig.1i). As an additional test of this finding, we considered that the nematic phase can also be characterized by the presence of a two-fold orientational order ( $\psi_2$ , defined in Eq. (3)), which captures the  $180^\circ$  rotational symmetry (see the Materials and Methods for a definition and the method of calculation). We found that many cells in the notochord region have a large  $\psi_2$  ( $> 0.5$ , see the dashed rectangle in Supp. Fig.3e). By this measure, the cells in the notochord region are more ordered than the cells on either side in a two-dimensional projection (see Supp. Fig.3f). Together these data revealed that the zebrafish notochord displays liquid crystal-like features during CE and prompted a more thorough investigation.

### **Nucleation and expansion of the nematic phase.**

Cell shape and alignment change over time during CE, so we next sought to characterize the development of nematic order in space and time as CE proceeds. To this end, we assessed the correlation between the shape index  $SI$  and the nematic order parameter  $S$  and the spatial and temporal dependencies of the two. At early times, when there are no observable changes in  $SI$  along the mediolateral axis (Supp. Fig.4a-b), a dome-like shape appears in  $S$  along the same axis, indicating the presence of a nematic phase in the mediolateral region (see Supp. Fig.4d), suggesting that changes in orientational order precede changes in cell shape.

The ordered phase in the middle region is stable, with only minor fluctuations in the standard deviation ( $\sigma_S$ ) (see Supp. Fig.4e between the red dashed lines and Supp Fig.4f-h at different times), in contrast to the larger fluctuations in the more disordered region on either side. Intriguingly, the cells in the nematic phase (enclosed by the two dashed lines) eventually form the zebrafish notochord (Supp. Fig.4c cyan dashed box). Hence, cells alter their orientational order much earlier in the CE, when differences in the cell shape are still quite subtle (Supp. Fig.4a-b), and the ordered notochord structure is not fully established. In summary, in the zebrafish notochord,  $S$  and its dispersion,  $\sigma_S$  (see more detailed discussion below) provide a better prediction of structural outcomes that produce observable changes in cell anisotropy.

To further probe the dynamics of the cell orientation order, we calculated the time dependence of the nematic order ( $S(t)$ ) for the cells in the notochord region (see Fig.1j). Instead of a slow increase in the cell shape with time, the value of  $S$  grows rapidly in the first hour and then increases slowly. Therefore, the tissues rapidly form a nematic phase at early times. The fluidity of a liquid crystal may facilitate both the CE process and the formation of the notochord (see Video III and Supp. Fig.5 in  $SI$  for the evolution of cell orientation). Unlike in synthetic liquid crystals<sup>26</sup>, the  $SI$  of cells increases with time, and there is active cell movement (see the cell trajectories in solid lines in Supp. Fig.4c), which may also contribute to the rapid formation of the nematic liquid crystal phase observed in Fig.1j. These results show that an ‘active’ nematic phase develops during zebrafish CE, in which the order parameter  $S$ , together with its dispersion  $\sigma_S$  describe the phase transition in notochord tissues.

To investigate the nematic order in the notochord region, we calculated the spatial correlation  $C_S(r)$  which describes how the alignment of cells varies with distance in the system. An exponential decay of the function indicates that alignment weakens quickly as cells get further apart. However, if  $C_S(r)$  decreases slowly, following a power-law pattern, it suggests there is significant alignment even between cells that are far apart, indicating long-range order in the orientations. The spatial correlation  $C_S(r)$  is defined as,

$$C_S(r) = \langle S(r+r_i) S(r_i) \rangle / \langle S(r_i) S(r_i) \rangle, \quad (2)$$

where  $S(r_i)$  is the nematic order (defined in Eq. (1) without averaging) of the cell at location  $r_i$ , and the average is over all cells in the notochord region. Interestingly, the decrease in the correlation function (Eq. (2)) follows a power law,  $C_S(r) \approx r^{-\alpha}$  (Fig.1k) with small value of  $\alpha$ , indicating the presence of a long-range spatial correlation in this region. The exponent,  $\alpha$ , changes in a time-dependent manner, but remains small (see Fig.1k) throughout, which

is consistent with the finding that the nematic order in the notochord region emerges early in the CE process (Fig.1f, i).

Finally, we investigated how such a nematic phase grows and propagates during CE. In Fig.1l, we plot the heatmaps of the order parameter  $S$  in (i)-(viii) at successive growth phases. A small “nucleus” with high  $S$  values (see the black region) forms at  $t=3$  min in the center of the field of view in (i). With time, this ordered phase starts to grow and expand in both the mediolateral and anteroposterior directions, with a more pronounced expansion in the latter direction. The boundary of the ordered phase (in black) is initially irregular (see (i)-(v)). At later times, a more regular rectangular region forms, representing the zebrafish notochord (see (vi)-(viii)). These data reveal that the formation of the zebrafish notochord is accompanied by the growth and propagation of a nematic phase starting from a small seed, reminiscent of a nucleation and growth process observed in crystals<sup>27</sup>. Observation of a nematic liquid crystal phase during zebrafish CE was striking and pushed us to determine if this liquid crystal state is an evolutionarily conserved feature of CE.

### **Evolution of anisotropic cell shape during *Xenopus* CE.**

We next asked if a nematic order phase was also present during *Xenopus* gastrulation. Like zebrafish, *Xenopus* notochord cells undergo CE. Unlike zebrafish, which have an optically accessible notochord, the *Xenopus* notochord is embedded within opaque tissues and is studied *ex vivo* using explant culture<sup>28-29</sup>. The *Xenopus* notochord is also initially much broader than zebrafish and takes 8-10 hours to narrow. Here, we visualized the onset of CE and thus the entire field of view is composed of notochord cells (Fig.2a-b, Supp. Fig.6a-f).

We collected time-lapse movies of *Xenopus* CE and applied  $SI$  to the cells. At early times *Xenopus* presumptive notochord cells (Fig.2a) are much more irregular than zebrafish (Fig.1a). Then all the cells in the broad notochord increase in anisotropy as illustrated by both the shape index ( $SI$ ), and the aspect ratio during CE (Supp. Fig.6g-h) and Video IV). The time dependence of  $SI$  for the cells in the field of view shows that it increases slowly with time ( $t$ ), and subsequently begins to grow faster (by about 30%) after  $t=70$  min (see the orange and red lines in Fig.2c). These data indicate that as for the case with zebrafish,  $SI$  can capture the rapid emergence of order in the tissue in advance of overt elongation of cells and thus is a useful metric.

### **The nematic liquid crystal phase is conserved in *Xenopus*.**

In *Xenopus* there is clear evidence of orientational order at very early times (see Fig.2d-f), though differences are seen along the anteroposterior axis. For example, most of the cells located at the anterior (top) of Fig.2d are oriented along the mediolateral axis and the orientational order parameter  $S$  in this region approaches unity (Fig.2e). This is consistent with previous observations that CE progresses from anterior to posterior<sup>15</sup>. As one moves posterior, there is a region of mixed polarity, followed by a second region of mediolateral orientation, while more posterior cells are more randomly oriented. It follows that the cells in *Xenopus* tissue also start to form a nematic liquid crystal even at early times of CE, although the cells have irregular shapes and appear to be randomly packed (see Supp. Fig.6a). Such an ‘active’ nematic phase could contribute to the self-assembly of ordered tissue structures, exhibiting both fluid and solid-state like properties.

Subsequently, almost all cells align along the mediolateral axis (Fig.2b)<sup>15</sup>, and form a near perfect nematic phase (see Fig.2g-i). Development of the nematic order is also captured by the time dependence of  $S$  for the cells in the field of view (see Fig.1j). The value of  $S$  increases rapidly after a short waiting period. Interestingly, such a fast growth behavior in *Xenopus* can be described by a similar function form as in zebrafish (compare the solid line and function listed in Fig.1j and 2j). The correlation function,  $C_S(r)$  (see Fig.2k), also exhibits a power-law behavior at all times, which indicates the presence of a long-range correlation for  $S$  in the nematic ordered phase. Taken together, the data suggest that the notochord rapidly forms a nematic phase with establishment of a long-range spatial order at early times during CE in both fish and frogs.

To better understand the spatio-temporal evolution of such a nematic phase, we calculated the heatmaps of  $S$  at different times (see Fig.2l). Just as in zebrafish tissue (Fig.1l), a small domain with an ordered phase initially forms at the right center of the field of view, and then begins to expand and propagate throughout the tissue in the field of view (see Fig.2l(i)-(viii)). The greater number of cells in the notochord of *Xenopus* may contribute to the less regular expansion process observed here compared to that observed in zebrafish. Our analyses reveal that a nematic phase emerges locally, then expands, in both zebrafish and *Xenopus* CE.

### **Evolution of anisotropic cell shape during *Drosophila* CE.**

Having found a nematic liquid crystal phase during gastrulation in two vertebrate organisms, we next asked if this behavior can be generalized to a more evolutionally distant animal. While many features of CE are conserved between *Drosophila* and vertebrates<sup>3</sup>, there are also significant differences. First, *Drosophila* CE occurs in the epithelial ectoderm in a region known as the germ-band<sup>30</sup>. Second, vertebrates and *Drosophila* employ different molecular mechanisms to pattern the converging and extending tissue<sup>7,31-32</sup>. Third, the *Drosophila* cells undergo pulsatile apical constrictions resulting in rapid changes in cell shape<sup>7</sup>. To ask if the physical principles of CE were evolutionarily conserved despite these molecular differences, we collected time-lapse movies of *Drosophila* CE and used  $SI$  to analyze cellular anisotropy.

Two snapshots of the *Drosophila* CE are shown in Fig.3a-b. The *Drosophila* tissue extended along the head-to-tail axis (that is the horizontal axis in Fig.3a-b). However, in contrast to zebrafish and *Xenopus*, cells elongated in the head-to-tail direction (see Fig.3b and Video V). To illustrate the cell shape changes during CE in *Drosophila*, we calculated the time dependence of  $SI$  for the cells in the dashed rectangle region in Fig.3b. Surprisingly,  $SI$  initially shows a decreasing behavior with time ( $t$ ). Then,  $SI$  starts to increase with time (see the orange and red lines in Fig.3c). In about 10 minutes, the  $SI$  abruptly reaches a high value and saturates ( $SI \approx 1.23$ ). Thus, *Drosophila* cells do reach an anisotropic state during CE, but the temporal dynamics are quite different from the other two species. More importantly, the orientation is flipped compared to the zebrafish and *Xenopus*. These differences prompted us to further explore nematic order during *Drosophila* CE.

### **Nematic order is conserved in *Drosophila*.**



In *Drosophila* embryo analyzed in this figure a small nematic domain appears at  $t=15$  minute (the upper left region in Fig.3a; cell orientation in Fig.3d) with  $S > 0.5$  (Fig.3e-f). At later times, the nematic order domain expands into the lower anterior region of the field of view and  $S$  increases further (see Fig.3g-i). We also calculated the time dependence of  $S$  for cells located in the dashed rectangle in Fig.3b. There is a rapid growth in  $S$  after a short time ( $<15$  minutes), as shown in Fig.3j. The growth of  $S$  could be fit by a function like that used in both zebrafish and *Xenopus* (see the functions shown in Fig.1j, 2j and 3j). The decay of  $C_S(r)$ , Eq. (2), found in *Xenopus* and *Drosophila* at early times ( $t < 40$  or 15 min, see Fig.2j and 3j) is faster compared to zebrafish, which is due to the onset of nematic order with lower values of  $S$  ( $< 0.5$ ) in the former two organisms at these times. However,  $C_S(r)$  exhibits a long-range spatial correlation, decaying as a power law ( $C_S(r) \sim r^{-\alpha}$ ) at all times for all three organisms (see Fig.1k, 2k, and 3k).

To further explore the spatial and temporal evolution of the nematic phase in *Drosophila*, we calculated the heatmap for the order parameter  $S$  at different times successively (Fig.3l). An ordered nematic phase emerges from the central anterior region, which grows and spreads to the posterior side of the field of view. We conclude that the appearance and growth of a nematic liquid crystal phase, consisting of a few tens to hundreds of cells on a length scale of hundreds of microns, is common to all three organisms.

Finally, to compare the three species on equal footing, we rescaled  $S(t)$ , and  $C_S(r)$ , by rescaling of  $t$  and distance  $r$  for each organism (see Fig.3m-n). Remarkably, all the data collapsed onto a single master curve (see the solid line in both figures). Thus, despite substantial biological differences in CE between flies and vertebrates<sup>3,33</sup>, our data suggest that a similar underlying physical mechanism operates in all three organisms during the development of the nematic ordered phase in CE. We next developed a minimal model to explore the conditions required for establishment of the nematic ordered phase we observed in zebrafish, *Xenopus*, and *Drosophila*.

### Theoretical model

To provide a quantitative explanation of these findings, we examined the minimal ingredients in a simple model (see Materials and Methods) that can explain the findings common to three species during CE: (i) Nematic order in the tissue forms by the creation of a domain that grows with time by a process that is reminiscent of nucleation and growth. (ii) The nematic order parameter  $S$  increases rapidly at early times and then slows down at later times, which can be described by  $S(t) = \Sigma - \Gamma t^{-\beta}$ , with  $\beta$  larger than zero (see Figs.1-3j).

We first devised a model with only near neighbor interactions in which the orientation of a cell is influenced by four nearest neighbors in a two-dimensional lattice. Such a short-range interaction could arise from cell-cell adhesive interactions, for example. Not unexpectedly, we found that while the near neighbor correlation does induce local order, it does not propagate beyond a short distance at subsequent times (Fig.4a-c). As a result, the nematic order parameter of the whole tissue is on average approximately zero (see Fig.4d). Thus, the near neighbor interaction model is not sufficient to explain our findings of CE, listed above.

Next, we considered a global cue, generating a model in which each cell is aligned in the same direction to simulate the effect of global cell alignment<sup>34</sup>. With this modification, we find that all the cells in the tissue eventually align globally in the same direction, forming a near-perfect nematic phase (Fig.4e-g). However, the formation and expansion of a small domain at early times that grows with time, which we observed experimentally in all three species, is not explained. This is because each cell changes its orientation independently due to the absence of local interactions among cells in the model (see also Fig.4e-f). In addition, the temporal evolution of  $S(t)$  grows linearly with time, which contradicts second finding listed above (compare Fig.1j and Fig.4h).

We then considered a third variant, which includes both local and global cell alignment (see Materials and Methods). This model recapitulated the growth behavior of nematic phases observed in experiments (see Fig.4i-k). Moreover, the simulations also predict the presence of topological defects as the tissue evolves, which is found in the experiments (see the blue lines in the nematic ordered region in Fig.1-3(g)). The temporal evolution of  $S(t)$  (see Fig.4l) also shows a rapid growth behavior, and the time-dependent growth is non-linear,  $S(t) = \Sigma - \Gamma t^{-\beta}$ , ( $\beta$  is larger than zero), both of which are consistent with experiments. Therefore, a minimal model with both local (arising from short range cell-cell interactions) and global (arising from long-range patterning) alignment of cells is sufficient to capture the nature of the nematic phase that is found in CE in three organisms.

### **Loss of Cdh3 inhibits the nematic phase in *Xenopus*.**

Next, we investigated the effect of disrupting short-range interactions by reducing cell-cell adhesion in *Xenopus*. To this end we knocked down Cdh3 (C-cadherin, P-cadherin in mammals), the classic cadherin expressed in the frog embryo, which is required for CE<sup>28,35</sup>. Upon knockdown of Cdh3 the cells are rounded (with smaller  $SI$  values, see Supp. Fig.7) compared to the wild type cells (see Fig.5a-b). There is no significant change in cell shape over the course of experiments (see Fig.5c and Video VI for a full 2-hour movie). Even the nematic order parameter  $S$  for cells in the field of view shows no obvious changes over time, except for fluctuating around zero (Fig.5d).

In addition, the values of  $S$  along different directions at different times, also show only small fluctuations around zero (Fig.5e-g, h-j). These data show not only that Cdh3 is required for cell anisotropy but also that short-range interactions are an essential permeator for nematic phase formation in vivo.

### **Loss of *spadetail* (*spt/Tbx16*) results in a collapse of the nematic phase in zebrafish.**

We then tested the validity of the theoretical model by disrupting another known molecular regulator of CE. *Spadetail* (*Spt*) encodes the transcription factor Tbx16, which is expressed in the paraxial mesoderm on each side of the notochord but is required for cell movements in the notochord itself<sup>36-38</sup>. We reasoned that this mutant might exert cell non-autonomous effects on convergent extension, especially at later stages. It may provide a proxy for the longer-range, global parameter in our model. We therefore analyzed nematic order in this mutant.

Comparison of representative snapshots of the *spt*-mutant and wild-type zebrafish tissues (see Fig.5k-l), the mutant tissue lacks notochord boundaries as expected<sup>38</sup>. And in the region where we expected to see the anisotropic notochord cells, we observed a stripe of highly constricted cells (see the dashed rectangle region in Fig. 5k, and Video VII), which we predict to be the presumptive notochord cells. In addition, the time dependence of the cell shape,  $SI(t)$ , and order parameter,  $S(t)$ , of cells in the mutant tissue change non-monotonically with time (see Fig.5m-n). Initially,  $SI$  increases linearly with time and there is a rapid growth of  $S$  indicating the formation of a nematic phase. Unlike the control, however, after a short time, both  $SI$  and  $S$  begin to decrease rapidly. Although many cells initially align in the mediolateral direction, especially early in the time course (Fig.5o), there are many disordered regions scattered throughout the tissue. Thus, *Spt* tissue fails to display the near-perfect nematic order found in wild-type tissue (Fig.1g), and it appears similar to our simulations that lack global cell alignment (see Fig.4a-d).

At later times, the ordered region in the mutant also decreases (Fig.5r), leading to the decay of  $S(t)$  (Fig.5n). In addition, in the wild-type, the order parameter  $S$  has a peak in the presumptive notochord region (Fig.1f), and such a peak is absent in the *spt* mutant, either along the mediolateral or anteroposterior directions at early or late times (Fig.5p-q, s-t). Although the *spt*-mutant tissue shows some degree of nematic order in certain regions, it is substantially weakened compared to the notochord region in wild-type. These findings show that disruption of global patterning, but not local cell interactions, alters the formation and maintenance of the nematic order phase.

### **Evaluating the mutants with the theoretical model.**

To further validate our model, we investigated whether it could also explain the two mutant experiments. First, we examined the results of the *Cdh3* knockdown in *Xenopus laevis* CE. We expect that cell-cell adhesion induced by *Cdh3* would influence the local cell alignment. By changing the parameter for the local cell interaction, parameter  $\mathcal{A}$  in Eq.(7) to a much smaller value (2500 times smaller) than that of the wild-type (see Supp. Table I), with a mild reduction of the global parameter  $\mathcal{B}$  in the same equation (one third of the value of wild-type), our model gives results similar to those observed in experiments (see Fig.6a-d). Therefore, our model suggests that the disruption of the nematic phase caused by the knockdown of C-cadherin in *Xenopus* results primarily from disruption of short-range interactions.

If loss of *Spt* reflects changes in the global parameter in our model, then we expect that changing this parameter will allow the model to recapitulate the pattern of nematic order observed in the mutants. We therefore changed the sign of the global parameter in our model (Model (iii) in Materials and Methods) after  $t = 1,000$  time steps, see Fig.6e-h), which has the effect of disrupting the cell alignment along the horizontal axis. We observed an increase in the ordered phases for some time after switching this parameter. As the tissue evolves, it starts to become more disordered and the order parameter  $S$  for the whole tissue also decreases (see Fig.6g-h), which is consistent with experimental findings in Fig.5n. Thus, by changing the value of the global order parameter, we can rationalize disruption of the nematic phase caused by the deletion of the *spt* gene. Taken together, a minimal theoretical model with both local and global cell alignment explains the nematic

phase formation in early gastrulation of zebrafish, *Xenopus* and *Drosophila*. Furthermore, the model is validated by our mutant experiments in which these two components are perturbed.

## Conclusion

We found that a nematic order phase arises during gastrulation in zebrafish, *Xenopus*, and *Drosophila*. All three organisms show a slow power-law decrease associated with the spatial correlation in the nematic order parameter, suggesting a conserved underlying tissue-level mechanism. Further, the nematic phase was established through a growth and propagation mechanism in each animal. However, there were interesting differences. For example, the orientation and time dependence of cellular anisotropy was strikingly different in *Drosophila* compared to the vertebrates. The properties of the nematic phase of the tissues allow them to flow like a liquid while maintaining orientational order<sup>39</sup>, which could be essential for their biological functions or may make tissues more robust to environmental perturbations. It is enticing to think nematic liquid crystal states may be universal to animal embryogenesis, and indeed the cellular process of convergent extension is conserved from flatworms to mammals<sup>2</sup>. Study of other animals is necessary to address this issue.

In addition, we did find some defects in the nematic liquid crystal phase of tissues. It will be interesting to investigate the relationship between these defects and mechanical properties of tissues properties in the so called “active liquid crystals”<sup>40-42</sup>. Thus, further studies are needed to search for liquid crystalline phases in biology at different scales and explore their possible biological significance<sup>43-48</sup>.

## Materials and Methods:

**Image analysis:** A single z-plane through live zebrafish, *Xenopus*, or *Drosophila* embryos expressing membrane EGFP (or mCherry), was selected for image analysis<sup>19</sup>. A minimum of two embryos was used for each organism and condition. The results are similar to the example shown in the figures. We first used “Cellpose”, a deep learning-based segmentation method<sup>49</sup>, to detect cell boundaries from snapshots of movies during zebrafish, *Xenopus* and *Drosophila* gastrulation (see Fig. 1(a)-(b), Fig. 2(a)-(b) and Fig. 3(a)-(b) for example). We then changed the image segmentation masks into gray scale images, which we used to track cells through ImageJ TrackMate plugin<sup>50</sup>. Finally, the position, area, perimeter, and the major and minor axes of cells are exported from TrackMate plugin for further analysis.

**Two-fold orientational order parameter  $\psi_2$ :** The n-fold orientational order parameter  $\psi_n$  is defined by<sup>51</sup>,

$$\psi_n(i) = \frac{1}{\sum_j l_{ij}^2} \sum_{j \in N(i)} l_{ij}^2 e^{in\theta_{ij}} \quad , (3)$$

where the sum is taken over all the nearest neighbors of the  $i^{\text{th}}$  cell,  $l_{ij}$  is the length of the edge shared between the Voronoi cells  $i$  and  $j$ , and  $\theta_{ij}$  is the angle between the vector pointing from cell  $i$  to  $j$ , and mediolateral axis (see the inset in Supp. Fig. 3(a)). Here, we consider  $n=2$ , the 2-fold orientational order parameter  $\psi_2$ , shown in Supp. Fig. 3(e)-(f).

**Models for the nematic phase during CE:** To rationalize the experimental findings, we introduce a simple two-dimensional lattice XY-type model. Each cell is located on a lattice site  $(i, j)$  (see Fig. 4(a)). The cells are allowed to change their orientation at each time step. Three variants of the model are considered, depending on the rules that govern how cells change their orientation.

**Model (i):** The cell orientation cell,  $\theta_i$  (the angle between the long axis of a cell and the horizontal axis), is influenced only by the orientation of four nearest (up, down, left, and right) neighbors. The temporal evolution of  $\theta_i$  is described by,

$$\frac{d\theta_i}{dt} = -\mathcal{A} \sum_j \sin(\theta_i - \theta_j), \quad (4)$$

where the summation is taken over the four nearest neighbors of cell  $i$ , and  $\mathcal{A}$  is a constant. That quartet of cells exchange neighbors via T1 transitions during CE is well known<sup>3,6</sup>. More recently<sup>52</sup>, vertex models have been used to describe this process theoretically, with focus on *Drosophila*. The goal of Model (i) is to assess the extent of order that arises due to short range cell-cell interactions involving a quartet of cell, without considering T1 processes explicitly.

**Model (ii):** Cell orientation,  $\theta_i$ , is only influenced by a global force field, leading to,

$$\frac{d\theta_i}{dt} = -\mathcal{B}\theta_i, \quad (5)$$

where  $\mathcal{B}$  is a constant. In this variant all the angles  $\theta_i$  evolve independently. In other words, there is complete absence of cooperativity, and the dynamics is controlled by the magnitude of  $\mathcal{B}$ .

**Model (iii):** In the third variant, the dynamic of  $\theta_i$ , is influenced by both the local cell ( $\mathcal{A}$ ) alignment and the global ( $\mathcal{B}$ ) fields, which leads to,

$$\frac{d\theta_i}{dt} = -\mathcal{A}\sum_j \sin(\theta_i - \theta_j) - \mathcal{B}\theta_i. \quad (6)$$

The Hamiltonian,  $\mathcal{H}$ , of the tissue is described by,

$$\mathcal{H} = \sum_i (-\mathcal{A}\sum_j \cos(\theta_i - \theta_j) + \frac{1}{2}\mathcal{B}\theta_i^2), \quad (7)$$

The models (i) and (ii) are special cases of Eq. (7). The first term in the above equation is taken from the two-dimensional X-Y model<sup>53</sup>, and the second term is similar as the energy term in the mean field Maier-Saupe theory<sup>54</sup>. To simulate the temporal evolution of each cell orientation using Eqs. (4)-(6), a uniform distribution for  $\theta_i$  ( $-\pi/2, \pi/2$ ) is applied initially. We used periodic boundary conditions in the simulations. A lattice size of  $20 \times 20$  is used in the main text. Different lattice sizes ( $30 \times 30, 50 \times 50$ ) are considered to check the finite size effect (see Supp. Fig.8-9). Almost the same results are found for the three models under different lattice sizes, indicating the absence of the finite size effect.

### **Zebrafish embryo manipulations, injections, and imaging:**

*Zebrafish strains and embryo staging:* Adult zebrafish were raised and maintained according to established methods<sup>55</sup> in compliance with standards established by the Washington University Animal Care and Use Committee. Embryos were obtained from natural matings and staged according to morphology as described<sup>56</sup>. All WT studies were carried out in animals of the AB background. Additional lines used include *spt*<sup>m423 57</sup>. Embryos of these strains generated from heterozygous intercrosses were genotyped by PCR after completion of each experiment.

*Microinjection of zebrafish embryos:* One-celled embryos were aligned within agarose troughs generated using custom-made plastic molds and injected with 1-3 pL volumes using pulled glass needles. Synthetic mRNAs for injection were made by *in vitro* transcription from linearized plasmid DNA templates using Invitrogen mMessage mMachin kits. 100 pg *membrane Cherry* (a kind gift from Dr. Fang Lin), or 50 pg *membrane eGFP* (7) mRNA was injected per embryo.

*Microscopy:* Live embryos expressing fluorescent proteins were mounted in 0.75% low-melt agarose in glass bottomed 35-mm petri dishes for imaging using a modified Olympus IX81 inverted spinning disc confocal microscope equipped with Voltran and Cobolt steady-state lasers and a Hamamatsu Imagem EM CCD digital camera. For time-lapse series, 60  $\mu\text{m}$  z-stacks with a 2  $\mu\text{m}$  step, were collected every three or five minutes for three or four hours using a 40x dry objective lens. Embryo temperature was maintained at 28.5°C during imaging using a Live Cell Instrument stage heater. When necessary, embryos were extracted from agarose after imaging for genotyping.

***Xenopus* embryo manipulations, injections, and imaging:** Embryos were acquired through in vitro fertilization. Female *Xenopus* were injected with 600 units of human chorionic gonadotropin and incubated overnight at 16°C. Eggs were then squeezed from the female *Xenopus* and fertilized. Eggs were dejellied two hours after fertilization using 3% cysteine (pH 8) and washed and reared in 1/3X Marc's Modified Ringer's (MMR) solution. Embryos were placed in 2% ficoll in 1/3X MMR for microinjections and then returned to 1/3X MMR 30 minutes after injections. A Parker's Picospritzer III and an MK1 manipulator were used for microinjections. Four-cell embryos were injected in the dorsal blastomeres to target the presumptive dorsal marginal zone. Membrane-RFP mRNA was injected at a concentration of 100pg per blastomere. Cdh3 morpholino was injected at a concentration of 10ng per blastomere. For dissections, stage 10.25 embryos were moved to Danilchik's for Amy (DFA) medium and Keller explants were excised using eyelash hair tools. Explants were maintained in DFA following dissection and time-lapse movies were collected ~5 hours after dissection. Images were acquired using a Nikon A1R microscope with a two-minute time interval and at a z-depth of ~5µm into the explant (above the superficial surface/coverslip).

***Drosophila* embryo movies:** The movies analyzed were collected for and published in Sawyer et al. 2011<sup>58</sup>. Wildtype *Drosophila* embryos expressing DEcadherin-GFP under control of the ubiquitin promotor and myosin light chain-mCherry (= Spaghetti Squash [sqh]) were filmed during stage 7 of embryonic development. Live imaging was performed with a PerkinElmer (Waltham, MA) UltraView spinning disk confocal ORCA-ER camera, Nikon (Melville, NY) 60× Plan Apo NA 1.4 or 100× Plan ApoVC NA 1.4 objectives, and MetaMorph software (Molecular Devices, Sunnyvale, CA).

## Acknowledgements:

This work is supported by the National Science Foundation (grant no. PHY 2310639), the Collie-Welch Chair through the Welch Foundation (F-0019), and NICHD (grant no. R01HD099191).

## REFERENCES

- 1 Shindo, A. Models of convergent extension during morphogenesis. *Wiley Interdiscip. Rev. Dev. Biol.* 7, e293 (2018).
- 2 Walck-Shannon, E., & Hardin, J. Cell intercalation from top to bottom. *Nat. Rev. Mol. Cell Biol.* 15, 34-48 (2014).
- 3 Huebner, R. J. & Wallingford, J. B. Coming to consensus: a unifying model emerges for convergent extension. *Dev. Cell* 46, 389–396 (2018).

- 4 Williams, M. L. & Solnica-Krezel, L. Cellular and molecular mechanisms of convergence and extension in zebrafish. *Curr. Top. Dev. Biol.* **136**, 377–407 (2020).
- 5 Keller, R., & Sutherland, A. Convergent extension in the amphibian, *Xenopus laevis*. *Curr. Top. Dev. Biol.* **136**, 271-317 (2020).
- 6 Sutherland, A., Keller, R., & Lesko, A. Convergent extension in mammalian morphogenesis. *Semin. Cell Dev. Biol.* **100**, 199-211 (2020).
- 7 Paré, A. C., & Zallen, J. A. Cellular, molecular, and biophysical control of epithelial cell intercalation. *Curr. Top. Dev. Biol.* **136**, 167-193 (2020).
- 8 Collinet, C., & Lecuit, T. Programmed and self-organized flow of information during morphogenesis. *Nat. Rev. Mol. Cell Biol.* **22**, 245-265 (2021).
- 9 Mongera, A. et al. A fluid-to-solid jamming transition underlies vertebrate body axis elongation. *Nature* **561**, 401-405 (2018).
- 10 Petridou, N. I., Grigolon, S., Salbreux, G., Hannezo, E. & Heisenberg, C.-P. Fluidization-mediated tissue spreading by mitotic cell rounding and non-canonical wnt signaling. *Nat. Cell Biol.* **21**, 169–178 (2019).
- 11 Ranft, J. et al. Fluidization of tissues by cell division and apoptosis. *Proc. Natl. Acad. Sci. USA* **107**, 20863–20868 (2010).
- 12 Malmi-Kakkada, A. N., Li, X., Samanta, H. S., Sinha, S. & Thirumalai, D. Cell growth rate dictates the onset of glass to fluidlike transition and long time superdiffusion in an evolving cell colony. *Phys. Rev. X* **8**, 021025 (2018).
- 13 Sinha, S., Malmi-Kakkada, A. N., Li, X., Samanta, H. S. & Thirumalai, D. Spatially heterogeneous dynamics of cells in a growing tumor spheroid: Comparison between theory and experiments. *Soft Matter* **16**, 5294–5304 (2020).
- 14 Bi, D., Yang, X., Marchetti, M. C. & Manning, M. L. Motility-driven glass and jamming transitions in biological tissues. *Phys. Rev. X* **6**, 021011 (2016).
- 15 Shih, J., & Keller, R. The epithelium of the dorsal marginal zone of *Xenopus* has organizer properties. *Development* **116**, 887-899 (1992).
- 16 Shih, J., & Keller, R. Cell motility driving mediolateral intercalation in explants of *Xenopus laevis*. *Development* **116**, 901-914. (1992)
- 17 Warga, R. M., & Kimmel, C. B. Cell movements during epiboly and gastrulation in zebrafish. *Development* **108**, 569-580 (1990).



- 18 Yen, W. W. et al. PTK7 is essential for polarized cell motility and convergent extension during mouse gastrulation *Development* **136**, 2039–2048 (2009).
- 19 Williams, M. L. & Solnica-Krezel, L. Nodal and planar cell polarity signaling cooperate to regulate zebrafish convergence and extension gastrulation movements. *eLife* **9**, e54445 (2020).
- 20 Park, J. A. et al. Unjamming and cell shape in the asthmatic airway epithelium. *Nat. Mater.* **14**, 1040-1048 (2015).
- 21 De Gennes, P. G., & Prost, J. The physics of liquid crystals. Oxford university press (1993).
- 22 Liu, K. et al. Thermotropic liquid crystals from biomacromolecules. *Proc. Natl. Acad. Sci. USA* **111**, 18596-18600 (2014).
- 23 Zemel, A., Rehfeldt, F., Brown, A. E. X., Discher, D. E., & Safran, S. A. Optimal matrix rigidity for stress-fibre polarization in stem cells. *Nat. Phys.* **6**, 468-473 (2010).
- 24 Trichet, L. et al. Evidence of a large-scale mechanosensing mechanism for cellular adaptation to substrate stiffness. *Proc. Natl. Acad. Sci. USA* **109**, 6933-6938 (2012).
- 25 Saw, T. B. et al. Topological defects in epithelia govern cell death and extrusion. *Nature* **544**, 212–216 (2017).
- 26 Schadt, M. Liquid crystal materials and liquid crystal displays. *Annu. Rev. Mater. Sci.* **27**, 305-379 (1997).
- 27 Markov, I. V. Crystal growth for beginners: fundamentals of nucleation, crystal growth and epitaxy. World scientific (2016).
- 28 Huebner, R. J. et al. Mechanical heterogeneity along single cell-cell junctions is driven by lateral clustering of cadherins during vertebrate axis elongation. *eLife* **10**, e65390 (2021).
- 29 Huebner, R. J. et al. Arvcf catenin controls force production during vertebrate convergent extension. *Dev. Cell* **57**, 1119–1131 (2022).
- 30 Irvine, K. D., & Wieschaus, E. Cell intercalation during *Drosophila* germband extension and its regulation by pair-rule segmentation genes. *Development* **120**(4), 827-841 (1994).
- 31 Butler, M. T., & Wallingford, J. B. Planar cell polarity in development and disease. *Nat. Rev. Mol. Cell Biol.* **18**, 375-388 (2017).
- 32 Lavalou, J., & Lecuit, T. In search of conserved principles of planar cell polarization. *Curr Opin Genet Dev.* **72**, 69-81 (2022).

- 33 Wallingford, J. B., Fraser, S. E. & Harland, R. M. Convergent extension: the molecular control of polarized cell movement during embryonic development. *Dev. Cell* **2**, 695–706 (2002).
- 34 Wallingford, J. B. Planar cell polarity and the developmental control of cell behavior in vertebrate embryos. *Annu. Rev. Cell Dev. Biol.* **28**, 627-653 (2012).
- 35 Lee, C. H., & Gumbiner, B. M. Disruption of gastrulation movements in *Xenopus* by a dominant-negative mutant for C-cadherin. *Dev. Biol.* **171**, 363-373 (1995).
- 36 Kimmel, C. B., Kane, D. A., Walker, C., Warga, R. M., & Rothman, M. B. A mutation that changes cell movement and cell fate in the zebrafish embryo. *Nature* **337**, 358-362 (1989).
- 37 Ho, R. K., & Kane, D. A. Cell-autonomous action of zebrafish *spt-1* mutation in specific mesodermal precursors. *Nature* **348**, 728-730 (1990).
- 38 Griffin, K. J., Amacher, S. L., Kimmel, C. B., & Kimelman, D. Molecular identification of *spadetail*: regulation of zebrafish trunk and tail mesoderm formation by T-box genes. *Development* **125**, 3379-3388 (1998).
- 39 Stephen, M. J., & Straley, J. P. Physics of liquid crystals. *Rev. Mod. Phys.* **46**, 617 (1974).
- 40 Saw, T. B. et al. Topological defects in epithelia govern cell death and extrusion. *Nature* **544**, 212–216 (2017).
- 41 Kawaguchi, K., Kageyama, R. & Sano, M. Topological defects control collective dynamics in neural progenitor cell cultures. *Nature* **545**, 327–331 (2017).
- 42 Zhang, R., Mozaffari, A. & de Pablo, J. J. Autonomous materials systems from active liquid crystals. *Nat. Rev. Mater.* **6**, 437–453 (2021).
- 43 Maroudas-Sacks, Y., Garion, L., Shani-Zerbib, L., Livshits, A., Braun, E., & Keren, K. Topological defects in the nematic order of actin fibers as organization centers of Hydra morphogenesis. *Nat. Phys.* **17**, 251-259. (2021)
- 44 Ou-Yang, Z.-C., Liu, J.-X. & Xie, Y.-Z. Geometric methods in the elastic theory of membranes in liquid crystal phases. *World Scientific* (1999).
- 45 DeCamp, S. J., Redner, G. S., Baskaran, A., Hagan, M. F. & Dogic, Z. Orientational order of motile defects in active nematics. *Nat. Mater.* **14**, 1110–1115 (2015).
- 46 Schaller, V., Weber, C., Semmrich, C., Frey, E. & Bausch, A. R. Polar patterns of driven filaments. *Nature* **467**, 73–77 (2010).

- 47 Morales-Navarrete, H. et al. Liquid-crystal organization of liver tissue. *eLife* **8**, e44860 (2019).
- 48 Doostmohammadi, A. & Ladoux, B. Physics of liquid crystals in cell biology. *Trends Cell Biol.* **32**, 140–150 (2022).
- 49 Stringer, C., Wang, T., Michaelos, M. & Pachitariu, M. Cellpose: a generalist algorithm for cellular segmentation. *Nat. Methods* **18**, 100–106 (2021).
- 50 Tinevez, J.-Y. et al. Trackmate: An open and extensible platform for single-particle tracking. *Methods* **115**, 80–90 (2017).
- 51 Cislo, D. J. et al. Active cell divisions generate fourfold orientationally ordered phase in living tissue. *Nat. Phys.* **19**, 1201–1210 (2023).
- 52 Brauns, F., Claussen, N.H., Wieschaus, E.F. and Shraiman, B.I., The Geometric Basis of Epithelial Convergent Extension. *eLife* **13**, RP95521 (2024).
- 53 Kosterlitz, J. M., and D. J. Thouless. Ordering, metastability and phase transitions in two-dimensional systems. *J. Phys. C* **6**, 1181-1203 (1973).
- 54 Maier, W., & Saupe, A. Eine einfache molekular-statistische Theorie der nematischen kristallinflüssigen Phase. *Teil II. Zeitschrift für Naturforschung A*, **15**, 287-292 (1960).
- 55 M. Westerfield, The zebrafish book. A guide for the laboratory use of zebrafish (*Danio rerio*). *University of Oregon Press*, (1993).
- 56 C. B. Kimmel, W. W. Ballard, S. R. Kimmel, B. Ullmann, T. F. Schilling, Stages of embryonic development of the zebrafish. *Dev Dyn* **203**, 253-310 (1995).
- 57 L. Solnica-Krezel et al., Mutations affecting cell fates and cellular rearrangements during gastrulation in zebrafish. *Development* **123**, 67-80 (1996).
- 58 Sawyer, J. K., Choi, W., Jung, K. C., He, L., Harris, N. J., & Peifer, M. A contractile actomyosin network linked to adherens junctions by Canoe/afadin helps drive convergent extension. *Mol. Biol. Cell* **22**, 2491-2508 (2011).

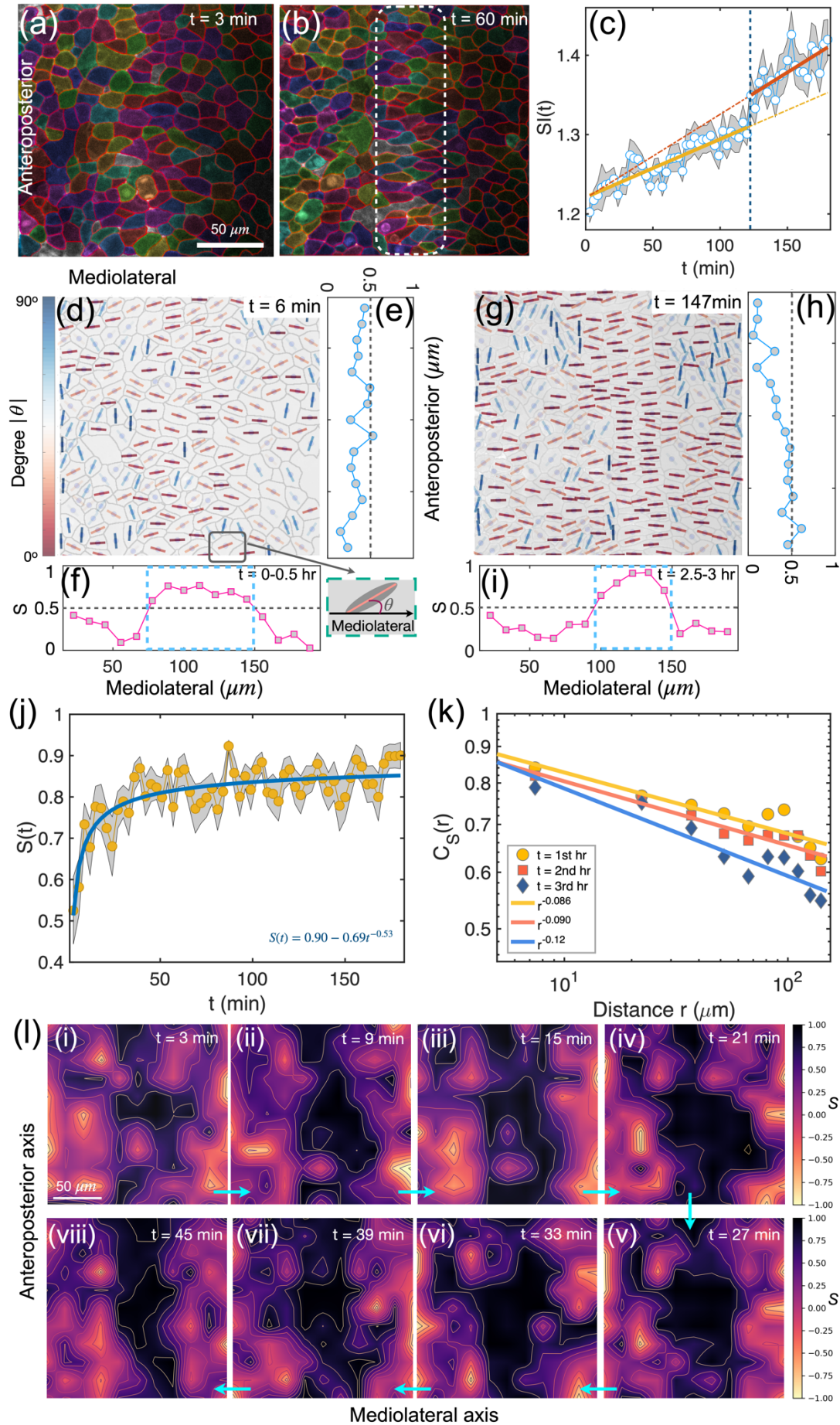


Figure 1. **Nematic order during zebrafish convergent extension (CE).** (a)-(b) Snapshots of zebrafish tissue at different times. The dashed rectangle in (b) shows the notochord location. The color associated with each cell is for illustration. (c) Temporal evolution of the shape index  $SI(t)$  of cells in the notochord region shown in (b). The orange and red lines are linear fits ( $SI(t)=7\times 10^{-4}t+1.22$ ,  $10^{-3}t+1.22$ ) with open circles (mean values), separated by the blue dashed line, where a jump in  $SI(t)$  occurs. The shaded area indicates the standard error of mean (SEM).  $n\approx 60$  cells from Video I. (d) Cell orientation, defined by the angle,  $\theta$ , between the long axis of cells (see the short lines) and the horizontal (mediolateral) axis of the embryo, (the inset at the bottom right of (d)) at  $t=6$  min. The short lines are color coded by the  $|\theta|$  value (a key is shown to the left of panel d). (e)-(f) The nematic order parameter,  $S$ , as a function of the cell position along the anteroposterior or mediolateral axis. Each curve is averaged over 10-time frames spanning 30 minutes. (g)-(i) Same as (d-f) except at later timepoints of CE. (j) Time dependent changes in  $S(t)$  of cells in the notochord region identified in (b). The solid line is a power-law fit ( $S(t)=0.9-0.69t^{0.53}$ ) with circles being the mean values. The shaded area shows the SEM. (k) The spatial correlation,  $C_S(r)$  (Eq. (2)), of cells in the notochord region at different times. The solid lines show a power-law decay. The functional forms of the decay are displayed in the figure. (l) (i)-(viii) The spatial-temporal evolution of  $S$  shows the propagation of the nematic order. Each figure in (i)-(viii) is averaged over two successive time frames (3-minutes interval). The scale bar in (a) and (l) is  $50 \mu\text{m}$ .

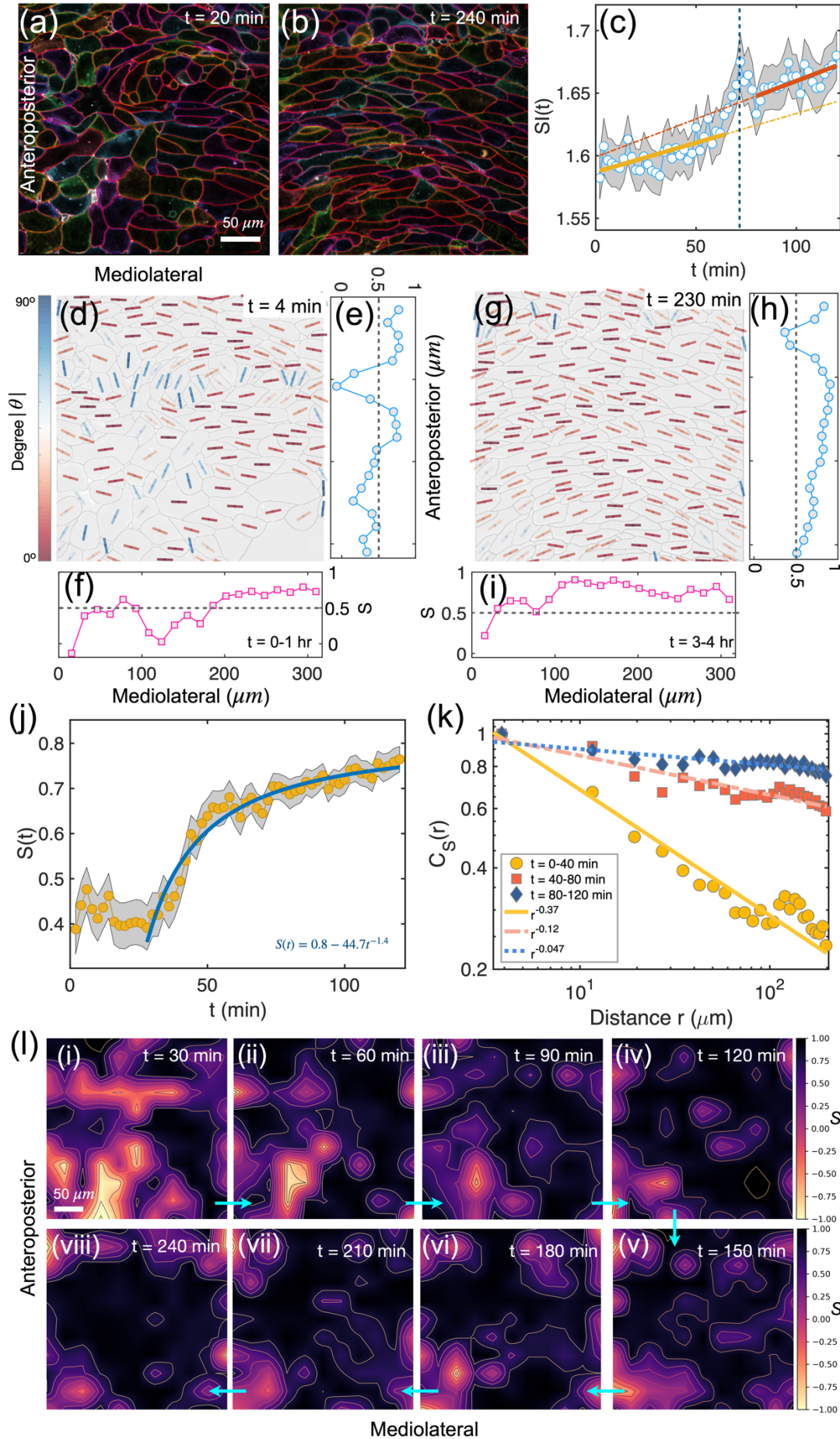


Figure 2. **Emergence of a nematic phase during *Xenopus CE*.** (a)-(b) Snapshots of *Xenopus laevis* tissue at different timepoints. (c) Time dependent changes in the shape index  $SI(t)$  of the notochord cells in the field of view. The orange and red lines are linear fits ( $SI(t)=4.7\times 10^{-4}t+1.59$ ,  $6.1\times 10^{-4}t+1.6$ ) with open circles (mean values). The data at early and late timepoints are separated by a jump (blue dashed line) in  $SI(t)$  at  $t=70$  min. The open circles give the mean  $SI$  values of all cells in the field of view at each time point. The shaded area shows the SEM.  $n\approx 200$  cells from Video IV. (d) Cell orientation in *Xenopus* tissues early during CE. The short lines are color coded by the value of  $|\theta|$  (defined in Fig. 1d.) (e)-(f) Nematic order parameter,  $S$ , as a function of the cell position along anteroposterior or mediolateral axis at an early timepoint. The two curves are obtained by averaging over 30 successive time frames spanning one hour. (g)-(i) Same as (d)-(f), except later. (j) Temporal evolution of the nematic order parameter  $S$  of cells in the field of view. The solid line is a power-law fit (functions listed in the figure) with circles (mean values). The shaded area shows the SEM. (k) Spatial correlation,  $S$ , of notochord cells at different times. Solid lines are a power-law fits (functions listed in the figure) of the data at different times. (l) (i)-(viii) Same as Fig.1(l), showing the propagation of the nematic order. Each figure in (i)-(viii) is averaged over three successive time frames (2-minutes interval). The scale bar in (a) and (l) is  $50\ \mu\text{m}$ .

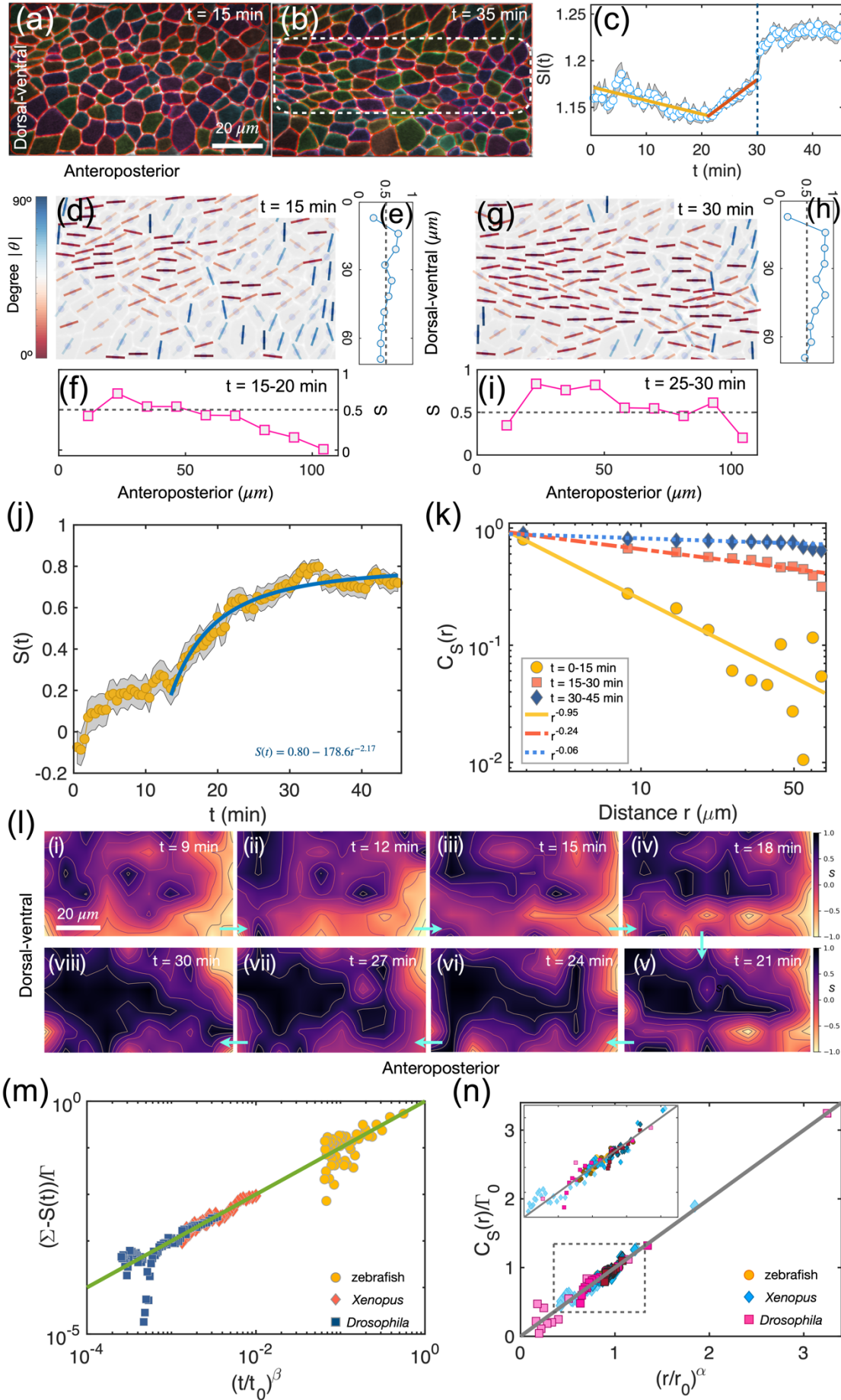




Figure 3. **Emergence of nematic order in *Drosophila* during CE.** (a)-(b) Representative snapshots of lateral views of the *Drosophila* germband. (c) Shape index  $SI(t)$  as a function of time for cells located in the dashed rectangle in (b). Linear fits ( $SI(t) = -1.5 \times 10^{-3}t + 1.17$ ,  $4.4 \times 10^{-3}t + 1.05$ ) with open circles (mean values) at different times, shown in orange and red. A jump (blue dashed line) occurs at  $t = 30$  min. The shaded area shows the SEM.  $n \approx 100$  cells from Video V. (d) Cell orientation is defined by the angle,  $\theta$ , between the long axis of cells (see the short lines) and the anteroposterior axis. The short lines are color coded by the value of  $|\theta|$ . (e)-(f) Orientational order parameter,  $S$ , as a function of the cell position along the dorsal-ventral, anteroposterior axis. The two curves are obtained by averaging over 10 successive time frames in five minutes. (g)-(i) Same as (d)-(f), except at later times. (j) Temporal evolution of the nematic order parameter  $S$  of cells in the dashed rectangle in (b). The solid line is a power-law fit ( $S(t) = \Sigma \Gamma t^{-\beta}$ , with functions listed in the figure) of the data with circles (mean values). The shaded area shows the SEM. (k) Spatial correlation of  $S$  for cells in the dashed rectangle in (b) at different times. The solid lines are a power-law fit ( $C_S(r) \propto r^{-\alpha}$ , with functions listed in the figure) at different times. (l) (i)-(viii) Same as Fig.1(l), it shows the propagation of the nematic order during *Drosophila* development. Each figure in (i)-(viii) is averaged over three successive time frames. (m) Scaled order parameter  $S$  as a function of the scaled time  $t/t_0$  ( $t_0 = 1$  min) for three organisms: zebrafish, *Xenopus*, and *Drosophila*. (n) Same as (m), except for the scaled spatial correlation of  $S$  over the scaled distance  $r/r_0$ .  $r_0$ , mean cell size, is taken by  $10 \mu\text{m}$  for zebrafish and *Drosophila*, and  $20 \mu\text{m}$  for *Xenopus*. The same symbol but in different colors represents data taken at different times for the same organism. The inset is a zoom-in view of the dashed box. The scale bar in (a) and (l) is  $20 \mu\text{m}$ .

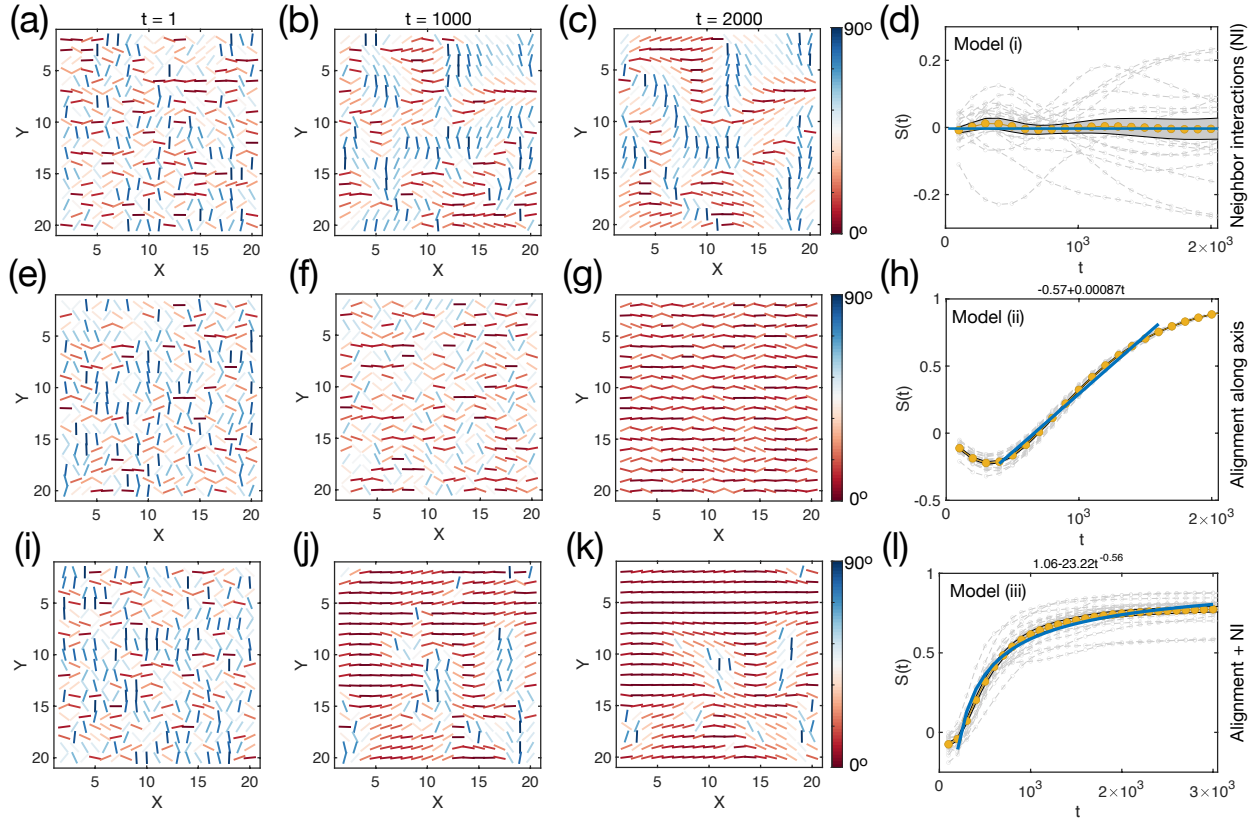


Figure 4. **Models for nematic order formation.** (a)-(d) Results from model (i) (Materials and Methods), where each cell orientation ( $\theta$ ) is influenced only by four neighbors. (a)-(c) Cell orientation at different times  $t$ . The parameter  $\mathcal{A} = 2.5 \times 10^{-3}$ . (d) Time dependent changes in  $S$  for all cells in (a). Each curve in gray represents one realization. Data in the brown dot is the mean value averaged over 20 trajectories. The shaded area shows the SEM. The solid line in navy blue corresponds to  $S = 0$ . (e)-(h) Results from model (ii), where each cell orientation is influenced only by a global field, leading alignment along the X-axis independently. The navy-blue line in (h) is a linear function, listed at the top of the figure. The parameter  $\mathcal{B} = 1 \times 10^{-3}$ . (i)-(l) Results from model (iii), Eq. (6). Navy blue line in (l) shows a power-law behavior with the function listed at the top of the figure. The values of  $\mathcal{A}$  and  $\mathcal{B}$  are  $2.5 \times 10^{-3}$ ,  $1 \times 10^{-3}$ , respectively.

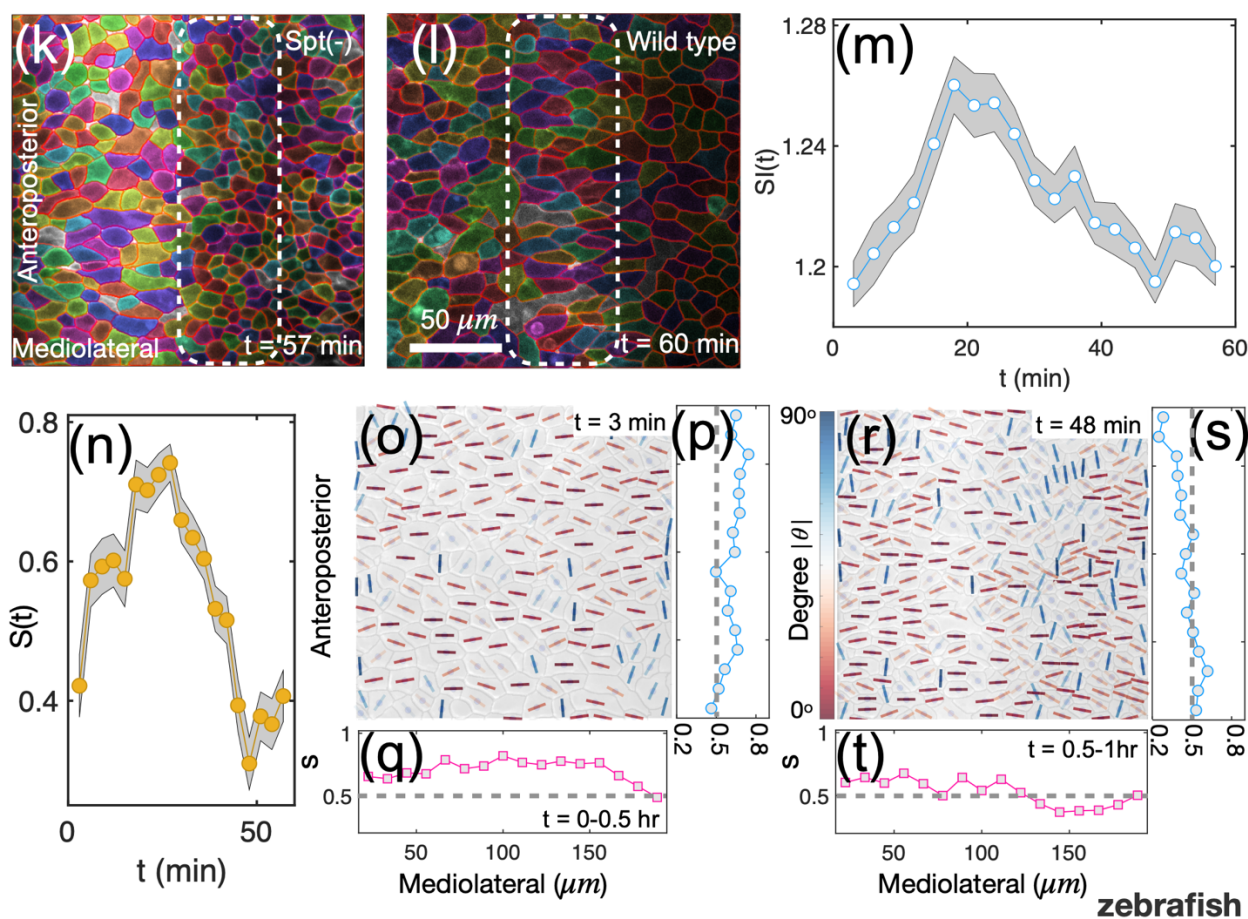
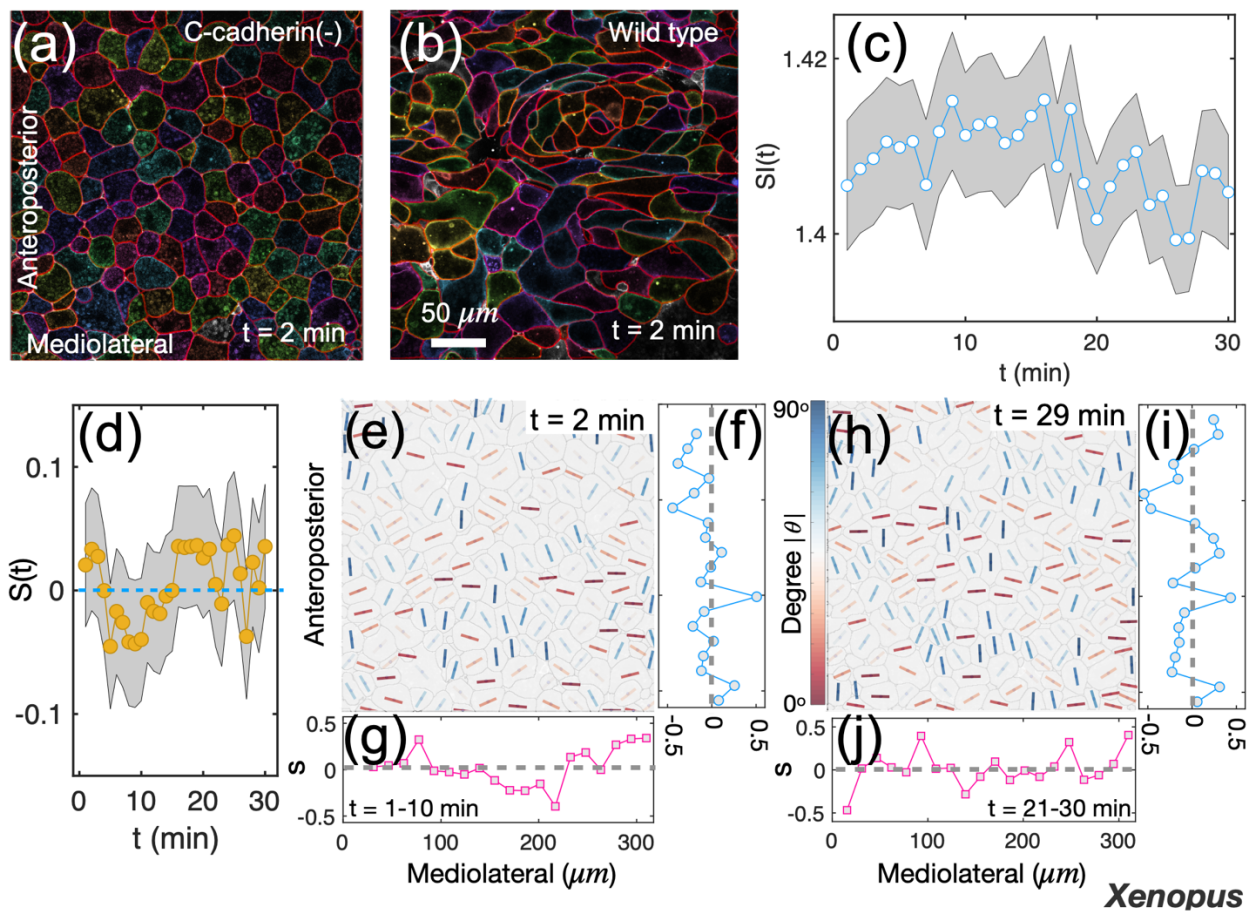


Figure 5. **Reduced nematic order in C-cadherin mutant Xenopus or spt mutant zebrafish.** (a)-(b) Two representative snapshots of C-cadherin knockdown or wild-type Xenopus tissue. (c), (d) Dependence of  $SI(t)$  and the nematic order parameter  $S(t)$  as a function of  $t$  in Xenopus tissue with C-cadherin knockdown. Open circles show the mean values, and the shaded area indicates the SEM.  $n \approx 200$  cells from Video VI. (e) Orientation of cells in Xenopus tissue (C-cadherin-) at an early timepoint. The short lines are color coded by the value of  $|\theta|$ . (f)-(g) Nematic order parameter,  $S$ , as a function of the cell position along the anteroposterior, mediolateral axis. Each curve is averaged over ten successive time frames spanning 10 minutes. (h)-(j) Same as (e)-(g), except at later timepoints. (k)-(l) Two representative snapshots of zebrafish tissue in spt-mutant or wild type. The dashed rectangle shows cells around the middle line. (m)-(n)  $SI(t)$  and  $S(t)$  as a function of  $t$  for the spt-mutant cells in the field of view. The mean (SEM) is shown in open circles (shaded area).  $n \approx 300$  cells from Video VII. (o) Cell orientation ( $\theta$ ) in zebrafish spt-mutant early times. (p)-(q) The orientational order parameter,  $S$ , as a function of the cell position along the anteroposterior, mediolateral axis at early times. Lines are averaged over ten successive time frames spanning 30 minutes. (r)-(t) Same as (o)-(q), except at later times. The scale bar in (b) and (l) is  $50 \mu\text{m}$ .

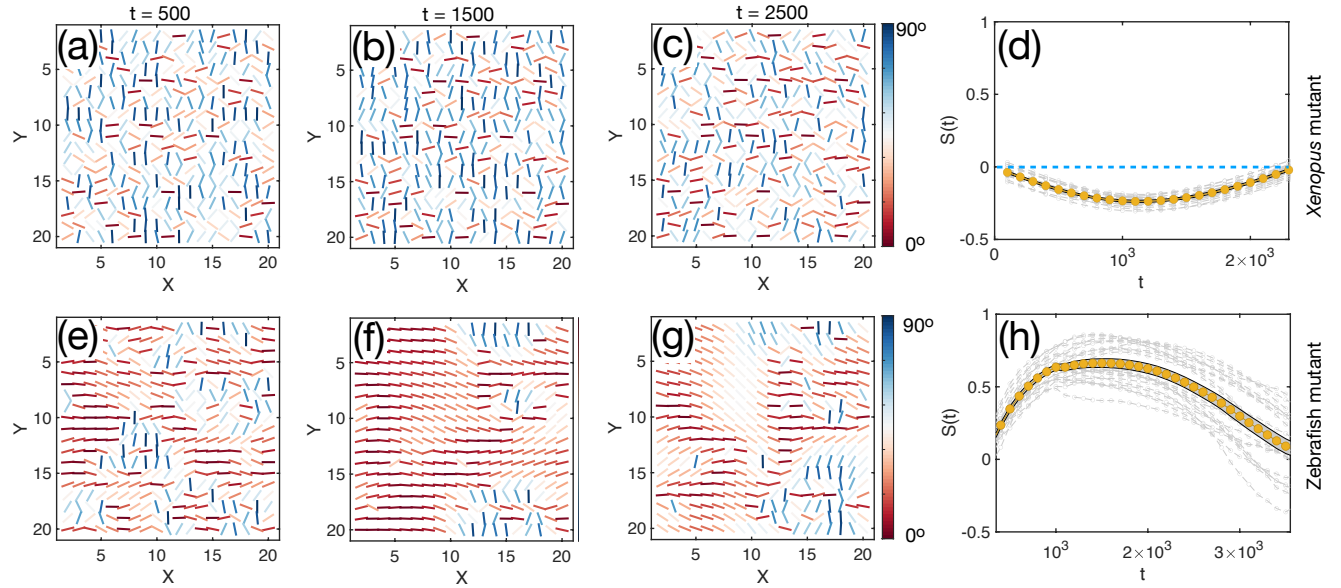


Figure 6. **Computational results for the mutant *Xenopus* and zebrafish tissues.** (a)-(c) The cell orientation ( $\theta$ ) in *Xenopus* mutants at different times. The short lines are color coded by the value of  $|\theta|$ . The parameter values are:  $\mathcal{A} = 10^{-6}$ , and  $\mathcal{B} = 3 \times 10^{-4}$  (see Eq. (7) in the main text). Time is measured in simulation steps. (d) The temporal evolution of the nematic order parameter  $S(t)$  of cells in mutant *Xenopus* tissues. Each curve in gray represents a single trajectory. Data in the brown dot is the mean value averaged over 20 trajectories. The shaded area shows the SEM. (e)-(h) Similar to (a)-(d) for zebrafish mutant tissues. The parameter values are:  $\mathcal{A} = 2.5 \times 10^{-3}$ , and  $\mathcal{B} = 1 \times 10^{-3}$  for  $t < 1000$ , while  $\mathcal{B} = -1 \times 10^{-3}$  for  $t \geq 1000$ .

**Emergence of cellular nematic order is a conserved feature of gastrulation in animal embryos - Supplementary Information**

Xin Li,<sup>1</sup> Robert J Huebner,<sup>2</sup> Margot L.K. Williams,<sup>3,4</sup> Jessica Sawyer,<sup>5,6</sup> Mark Peifer,<sup>6</sup> John B Wallingford,<sup>2</sup> and D. Thirumalai<sup>1,7</sup>

<sup>1</sup>*Department of Chemistry, University of Texas at Austin, Austin, TX 78712, USA*

<sup>2</sup>*Department of Molecular Biosciences, University of Texas at Austin, Austin, TX 78712, USA*

<sup>3</sup>*Center for Precision Environmental Health & Department of Molecular and Cellular Biology, Baylor College of Medicine, Houston, TX 77030, USA*

<sup>4</sup>*Department of Developmental Biology, Washington University School of Medicine, St. Louis, MO 63110, USA*

<sup>5</sup>*Department of Pharmacology and Cancer Biology, Duke University, Durham, NC 27710, USA*

<sup>6</sup>*Department of Biology, University of North Carolina at Chapel Hill, Chapel Hill, NC 27599-3280, USA*

<sup>7</sup>*Department of Physics, University of Texas at Austin, Austin, TX 78712, USA*

In the Supplementary Information (SI), we provide additional figures and explanations for the Videos that are pertinent to the results present in the main text.

### SI Figures

Figure S1. **Snapshots of the mesoderm layer of zebrafish tissues and spatial-temporal evolution of the cell shape index  $SI$  during  $CE$ .**

Figure S2. **Evolution of the cell area distribution in zebrafish.**

Figure S3. **Nematic order during zebrafish development.**

Figure S4. **Spatial-temporal evolution of nematic order during zebrafish development.**

Figure S5. **Evolution of cell orientation in zebrafish  $CE$ .**

Figure S6. **Cell morphology changes during *Xenopus*  $CE$ .**

Figure S7. **Comparison of cell shape index for wild-type *Xenopus* versus *C-cadherin* knockdown tissues.**

Figure S8. **Calculated nematic order formation using simulation lattice size  $30 \times 30$ .**

Figure S9. **Computational results using lattice size  $50 \times 50$ .**

### SI Table

Table I. **The parameters used in the simulation.**

### SI Videos

Video I. **Movie for zebrafish  $CE$ .**

Video II. **The evolution of the cell shape index ( $SI$ ) as a function of the cell position ( $x$ ) along the mediolateral axis of zebrafish in Video 1.**

Video III. **The evolution of the cell orientation in zebrafish  $CE$ .**

Video IV. **Movie for *Xenopus laevis*  $CE$ .**

Video V. **Movie for *Drosophila*  $CE$ .**

Video VI. **Movie for *Xenopus laevis*  $CE$  after *Cdh3* knockout.**

Video VII. **Movie for zebrafish  $CE$  with *spt/Tbx16* mutant.**

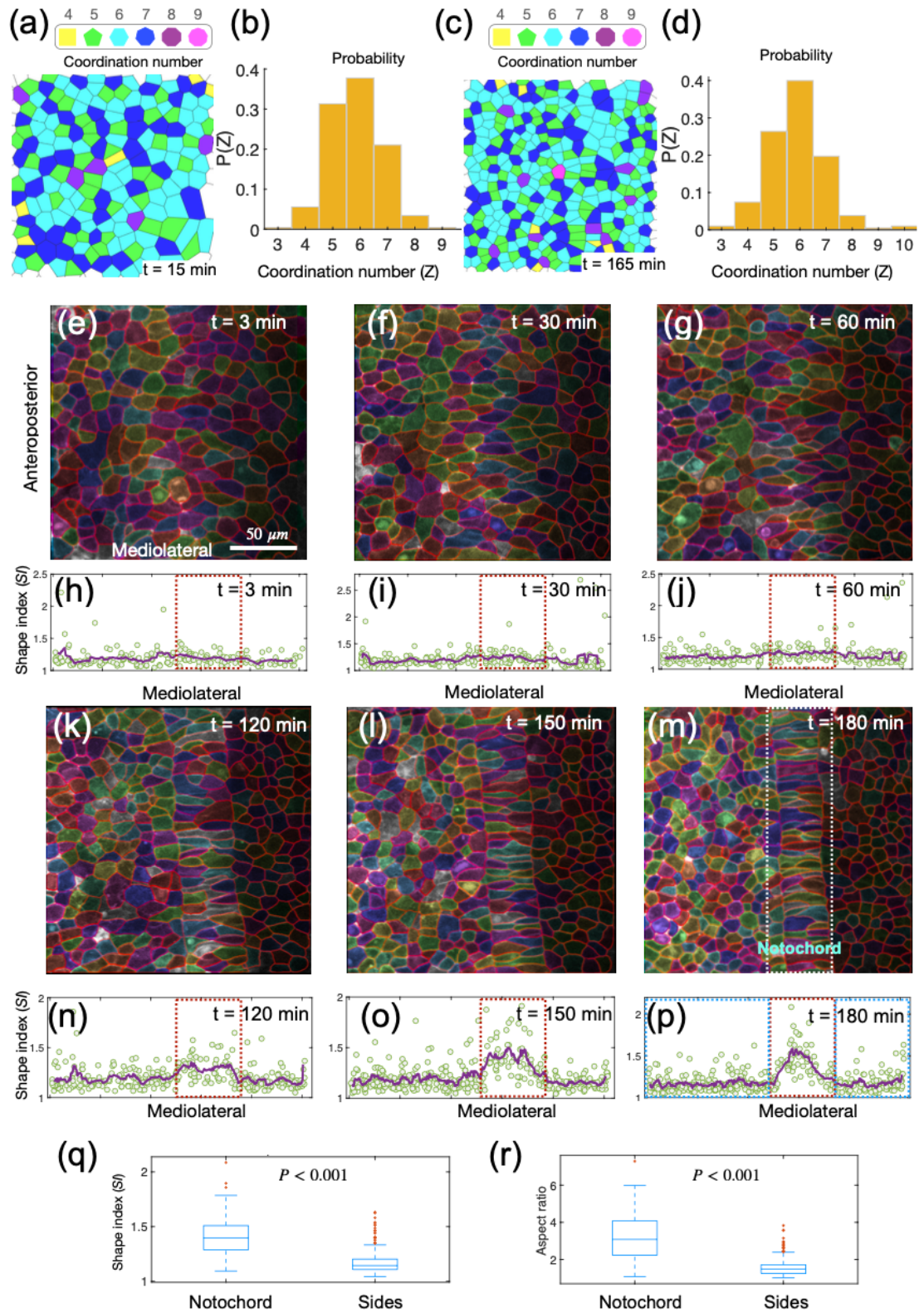




**FIG. S1: Snapshots of the mesoderm layer of zebrafish tissues and spatial-temporal evolution of the cell shape index  $SI$  during  $CE$ .** (a), (c) Snapshots of the mesoderm layer of zebrafish at different timepoints, with cells segmented, and cell coordination number  $Z$  (the number of neighbors), derived from Voronoi tessellation of the cell centers. Each Voronoi cell is displayed in a different color based on the value of  $Z$ , as listed by the polygon symbols at the top of (a), (c). (b), (d) The distribution of  $Z$  for cells in (a), and (c). (e)-(g) and (k)-(m) Snapshots of the zebrafish mesoderm layer at different times. Cell colors are for illustration purposes. (h)-(j) and (n)-(p) Shape index,  $SI \equiv \frac{P}{\sqrt{4\pi A}}$ , as a function of the cell position along the mediolateral axis corresponding to (e)-(g) and (k)-(m). (q) Box-plot of the  $SI$  of cells located in the notochord region (the red dashed box) versus cells at the two sides (the blue dashed box) in (p). (r) Same as (q), except showing the cell aspect ratio. The two-sided Mann-Whitney U test is used for the statistical analysis. The p-value is listed in (q) and (r).

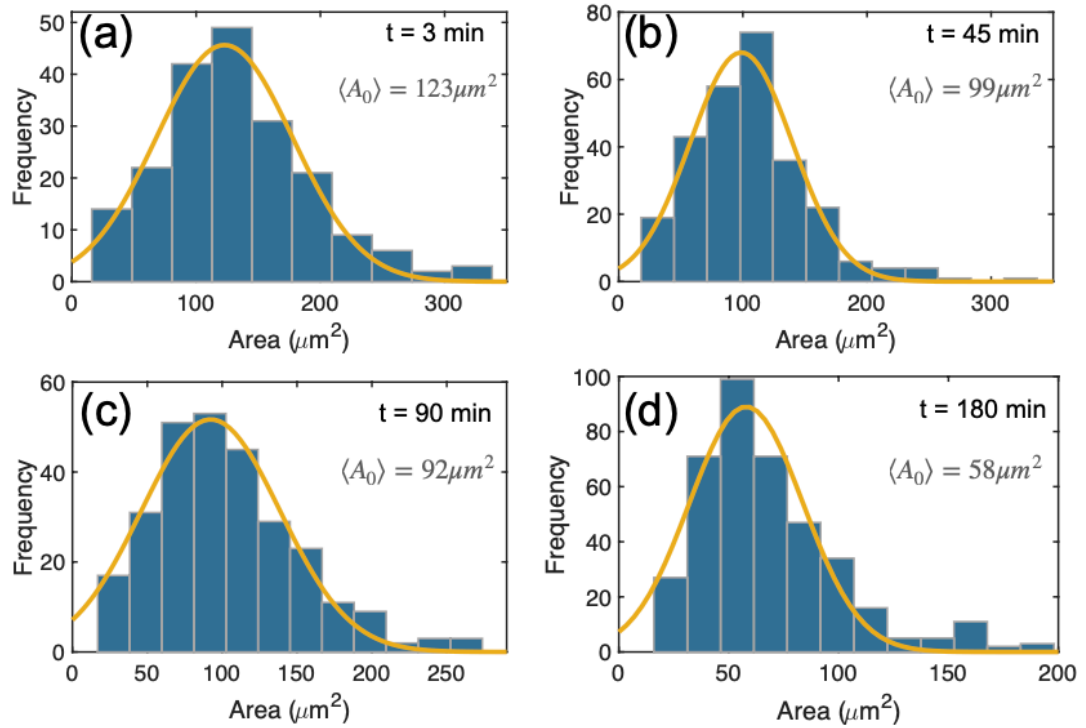


FIG. S2: **Evolution of the cell area distribution in zebrafish.** (a)-(d) Histogram of the apical cell area at different times during zebrafish *CE*. The solid line is the Gaussian fit to the data. The mean area,  $\langle A_0 \rangle$ , of cells from the Gaussian fit is listed in each figure.

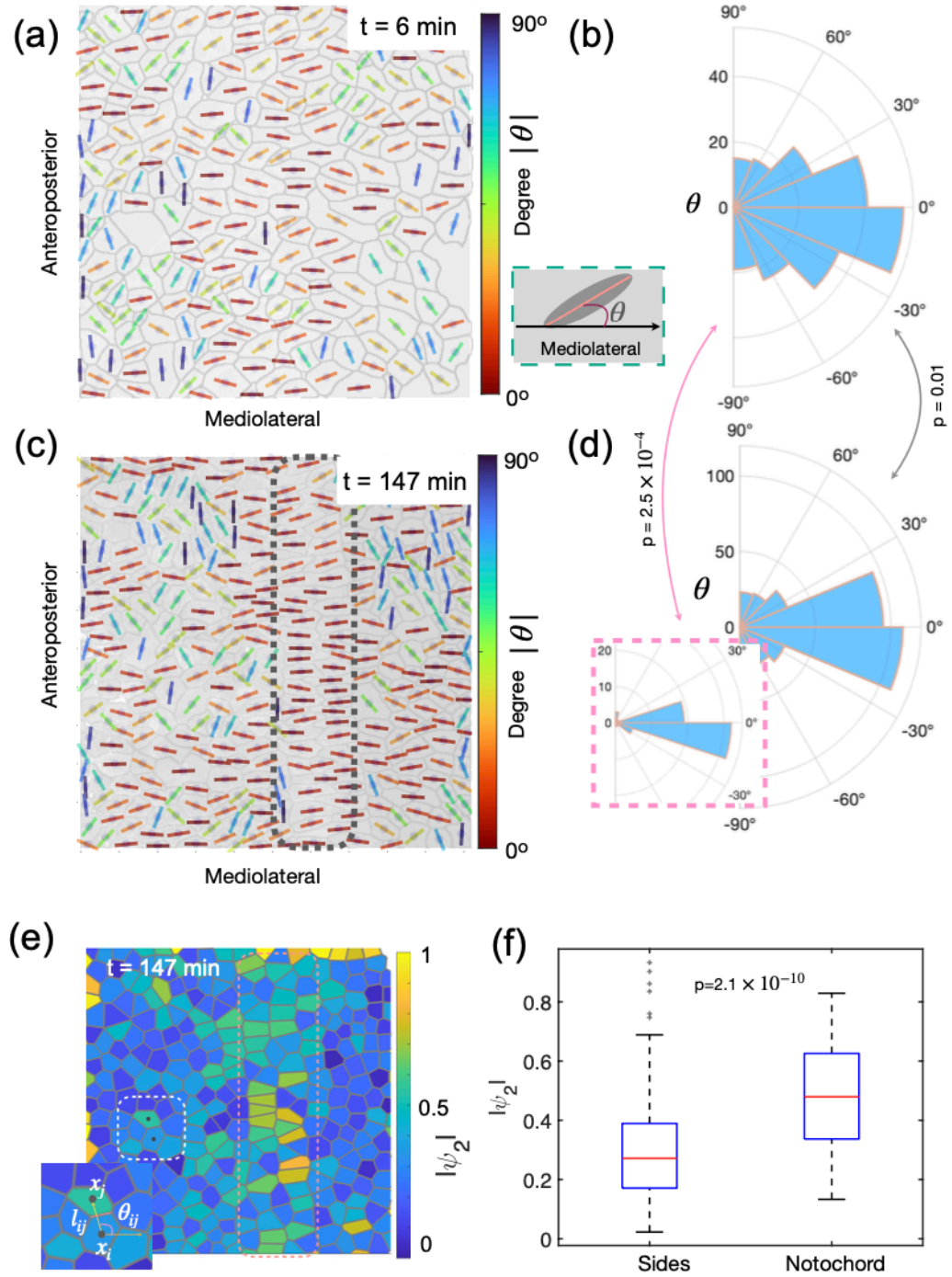


FIG. S3: Nematic order during zebrafish development.

**FIG. S3: Nematic order during zebrafish development.** (a) and (c) Same as Figs. 1(d) and (g) in the main text, showing the cell orientation in zebrafish tissues at different times. The cell orientation is defined by the angle,  $\theta$ , between the long axis of cells (see the short lines) and the horizontal (mediolateral) axis, as shown in the inset at the bottom right of (a). The short lines are color coded by the value of  $|\theta|$ . (b) Histogram of the polar angle  $\theta$  for all cells in (a). (c)-(d) Same as (a)-(b), except they are at a later timepoint. The inset in (d) gives the histogram of  $\theta$  for cells located in the notochord region shown by the pink dotted rectangle in (c). The p-values between the patterns in (b) and (d), (b) and the inset in (d) are calculated with two-sample Kolmogorov–Smirnov test. (e) The 2-fold orientation order,  $|\psi_2|$ , of cells (see the definition in Eq.(2) in the Materials and Methods section). Each Voronoi cell is color coded by the value of  $|\psi_2|$  (see the scale on the right). The inset on the left bottom is a zoom in of the white dashed rectangle region. The variables  $\theta_{ij}$  (the angle between the vector pointing from cell i to j) and  $l_{ij}$  (the length of the edge shared between the Voronoi cells i and j) are used in the definition of  $|\psi_2|$ . (f) Boxplot of  $|\psi_2|$  for cells located at two sides or the middle region (see the dotted rectangle in (g)). The p-value is calculated from the two-sided Mann-Whitney U test.

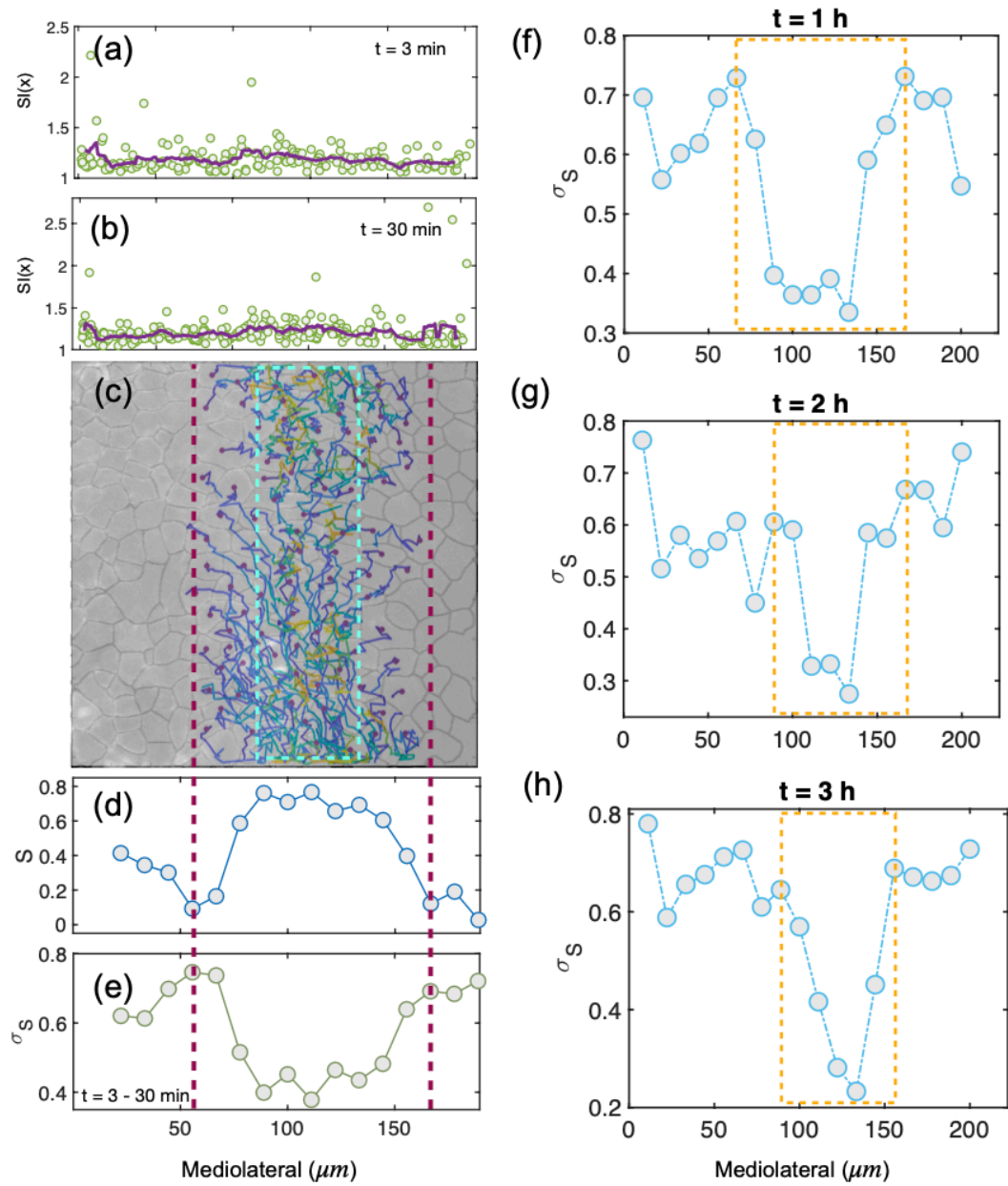


FIG. S4: Spatial-temporal evolution of nematic order during zebrafish development.

**FIG. S4: Spatial-temporal evolution of nematic order during zebrafish**

**development.** (a)-(b) The cell shape index,  $SI(x)$ , along the mediolateral axis at early timepoints. (c) The tissue snapshot at an early timepoint is overlaid with the trajectories of cells located inside of the red dashed lines over the next 3 hours, with blue color for early timepoints and yellow for late timepoints. The dashed rectangle in cyan gives the final notochord region. (d)-(e) The nematic order parameter,  $S$ , and the standard deviation,  $\sigma_S$ , along the mediolateral axis. The value of  $S$  and  $\sigma_S$  in (d)-(e) are averaged over 10 successive time frames ( $t=30$  minutes). The boundaries between the nematic-order and disordered regions are indicated by the red dashed lines. The cyan rectangle indicates the final location of the notochord region in zebrafish. (f)-(h) The spatial-temporal evolution of  $\sigma_S$ . A sharp transition of  $\sigma_S$  along the mediolateral axis is observed as indicated by the dashed rectangles at different times, and this region narrows over time.

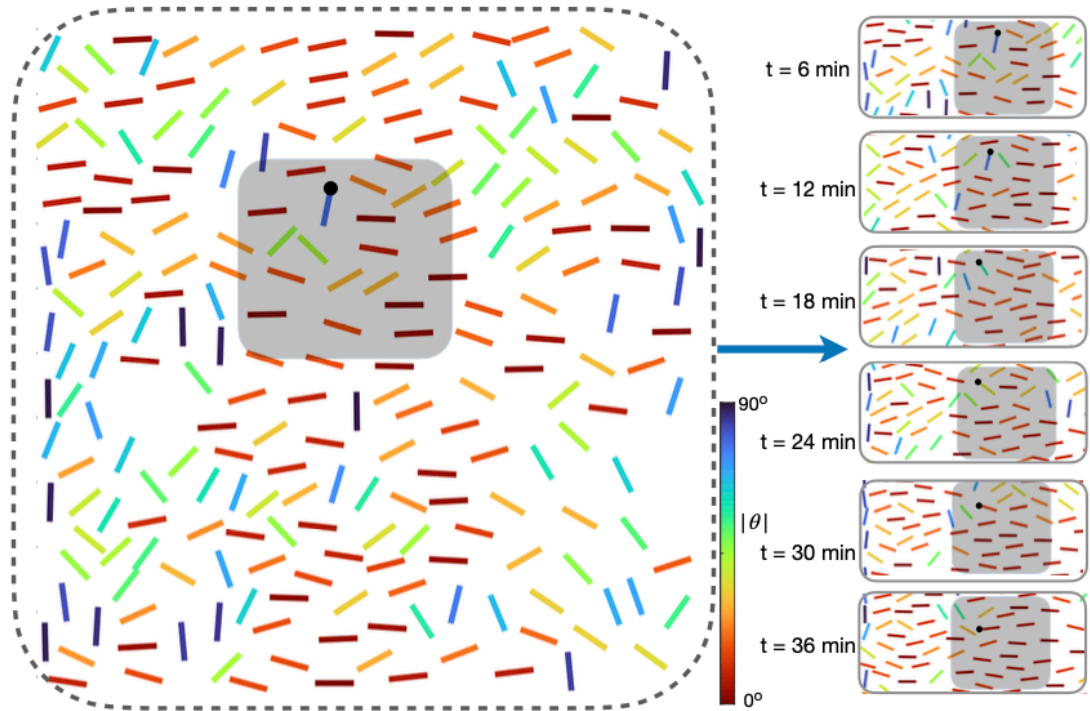


FIG. S5: **Evolution of cell orientation in zebrafish CE.** Similar to Fig. 1(d) in the main text. The cell orientation is defined by the angle,  $\theta$ , between the long axis of cells (see the short lines) and the mediolateral (horizontal) axis as shown in the inset in Fig. S3(a). The lines are color coded by the value of  $|\theta|$ . Figures on the right show the evolution of cell orientation located in the shaded area of the left figure. Individual cells change their orientation (see the line with a dot on one side as an example) and form a nematic phase.

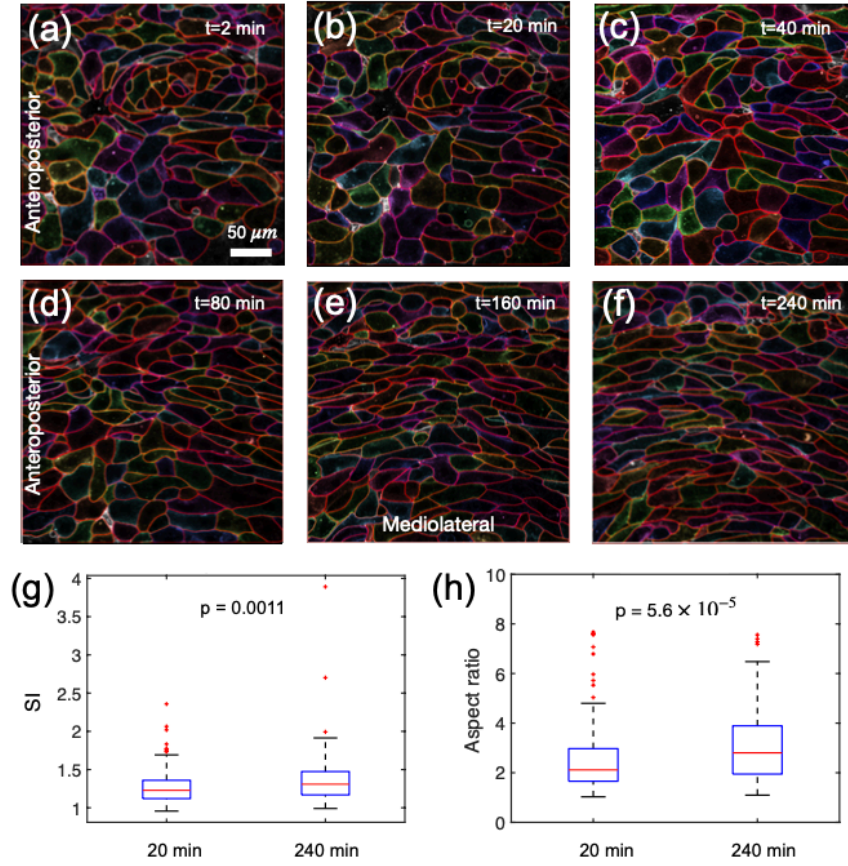


FIG. S6: **Cell morphology changes during *Xenopus CE*.** (a)-(f) Snapshots of *Xenopus laevis* tissues at different times during *CE*. (g) Box-plot of the *SI* value calculated for cells from (b) and (f). (h) Aspect ratio of cells from (b) and (f). The two-sided Mann-Whitney U test is used for the statistical analysis in (g)-(h). The p-value is listed in each figure.



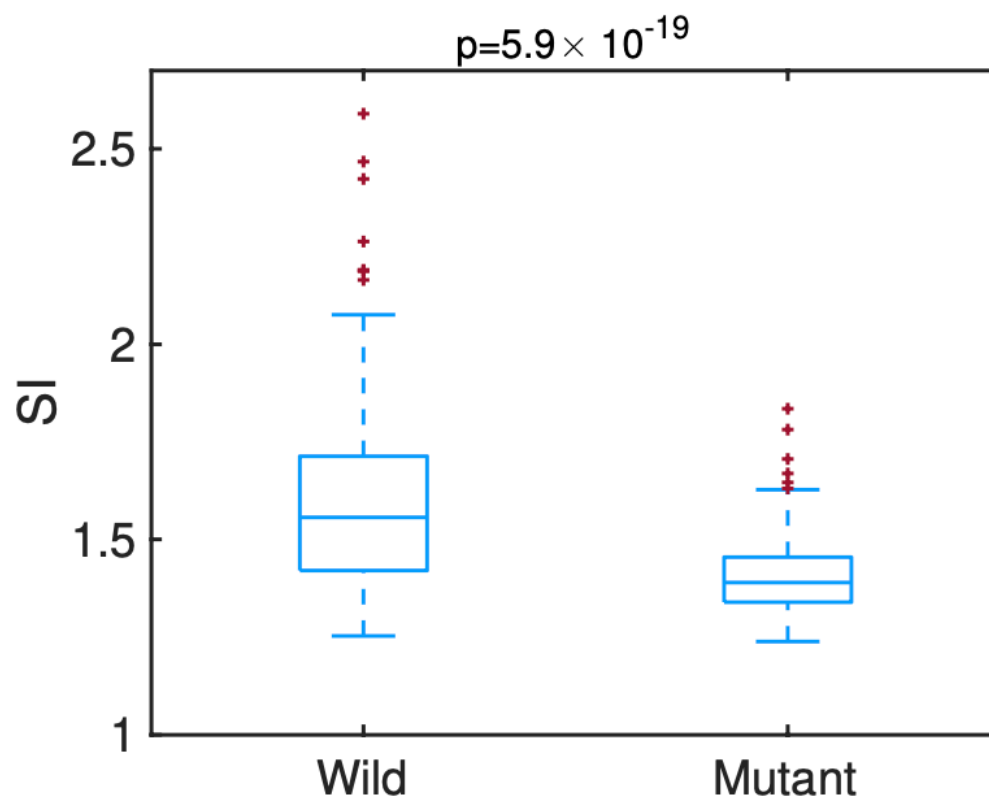


FIG. S7: **Comparison of cell shape index for wild-type *Xenopus* versus *C-cadherin* knockdown tissues.** Box-plot of the *SI* for cells from Figs. 4(k) and (l) for *C-cadherin* knockdown and wild-type *Xenopus* tissues. Mann-Whitney U test is used for the statistical analysis. The p-value is listed in the figure.

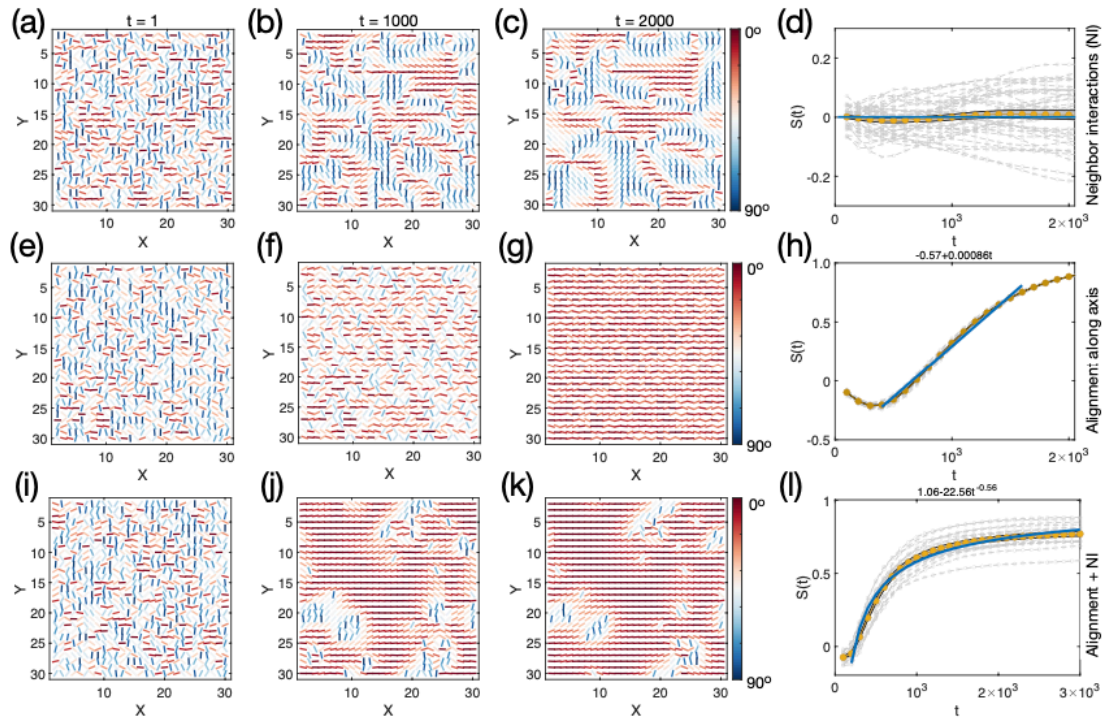


FIG. S8: Calculated nematic order formation using simulation lattice size  $30 \times 30$ . Same as Figure 4 in the main text, except the lattice size is  $30 \times 30$ . (a)-(d) Results from model (i). (e)-(h) Results from model (ii). (i)-(l) Results from model (iii). The parameter  $\mathcal{A} = 2.5 \times 10^{-3}$ ,  $\mathcal{B} = 1 \times 10^{-3}$ . The models are described in the main text.

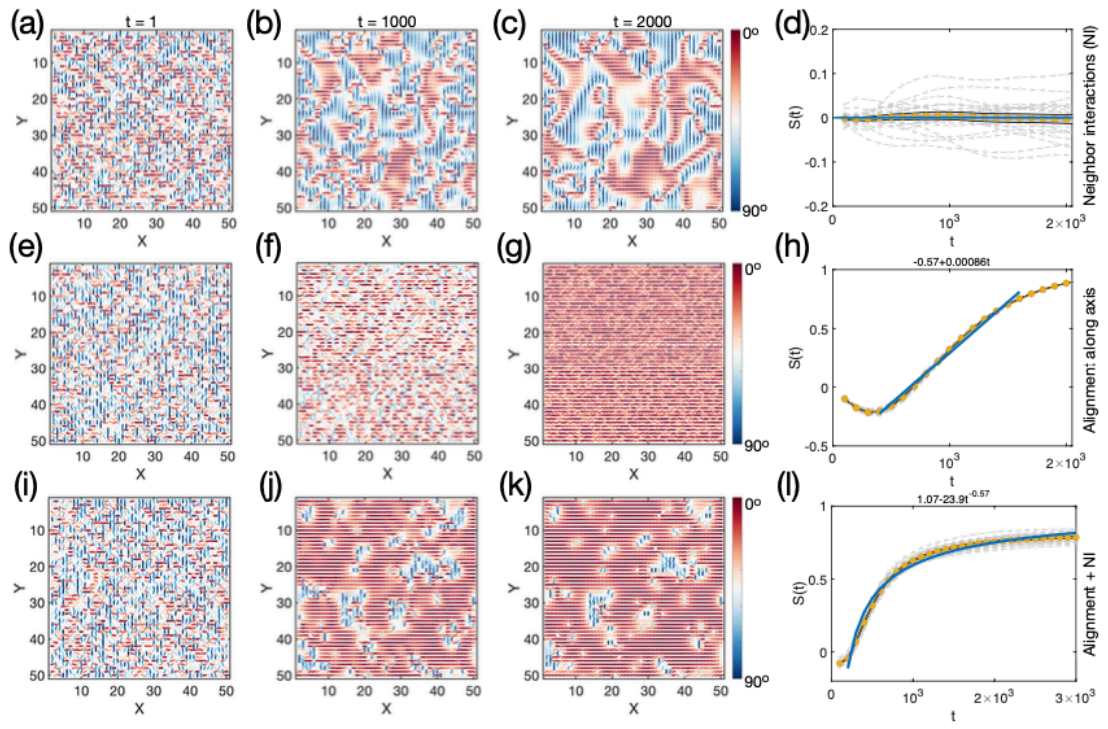


FIG. S9: Computational results using lattice size  $50 \times 50$ . Same as Figure S8, except the lattice size is  $50 \times 50$ .

TABLE I: The parameters used in the simulation.

<b>Models</b>	$\mathcal{A}(\text{local})$	$\mathcal{B}(\text{global})$
Model i	$2.5 \times 10^{-3}$	0
Model ii	0	$1 \times 10^{-3}$
Model iii	$2.5 \times 10^{-3}$	$1 \times 10^{-3}$
Model iii ( <i>Xenopus</i> mutant)	$10^{-6}$	$3 \times 10^{-4}$
Model iii (zebrafish mutant)	$2.5 \times 10^{-3}$	$-1 \times 10^{-3}$